Delft University of Technology

Aerodynamic Design of a Flying V Aircraft

Faggiano, Francesco; Vos, Roelof; Baan, Max; van Dijk, Reinier

Aerodynamic Design of a Flying V Aircraft

Francesco Faggiano[*] and Roelof Vos[†]

Delft University of Technology, 2629HS Delft, the Netherlands

Max Baan[‡] and Reinier van Dijk[§]

ParaPy B.V., 2629JD Delft, the Netherlands

A Flying V aircraft is a tailless, V-shaped flying wing with two cylindrical pressurized cabins placed in the wing leading edge and two over-the-wing engines. Elevons provide longitudinal and lateral control while two tip-mounted vertical tails double as winglets. The goal of the presented study is to estimate the lift-to-drag ratio of this configuration at the cruise condition: $M = 0.85$, $h = 13,000$m, and $C_L = 0.26$. A vortex-lattice method is used to rapidly investigate the feasible design space, whereas an Euler solver on an unstructured grid is adopted for a more accurate wave and vortex-induced drag estimation. The profile drag is computed by an empirical method. The NASA Common Research Model is adopted as a benchmark with an estimated lift-to-drag ratio of 18.9. The three-dimensional geometry of the Flying V is generated according to a multi-level parametrization: the planform shape is parametrized with 10 variables, five wing sections are identified and described by a total of 43 parameters, while the winglet planform is defined by 3 additional variables. After a multi-fidelity design space exploration, two design approaches are investigated: a dual-step optimization, where planform and airfoil variables are subsequently varied, and a single-step optimization, where planform and airfoil variables are varied simultaneously. The highest lift-to-drag ratio is attained with the single-step optimized configuration and amounts to 23.7. It is therefore concluded that the Flying V Aircraft can have a 25% higher lift-to-drag ratio than the reference aircraft.

Nomenclature

a	geometry coefficient ($\sim$)		p	static pressure (Pa)
A	aspect ratio ($\sim$)		S	wing (reference) area (m^2)
b	wing span (m)		S_{wet}	wetted area (m^2)
c	chord (m) or geometry coefficient ($\sim$)		T	air temperature (K)
C_D	drag coefficient ($\sim$)		W	weight (N)
C_L	lift coefficient ($\sim$)		W_F	oval cross section floor width (m)
C_m	pitching moment coefficient ($\sim$)		$\bar{y}$	variables vector ($\sim$)
C_n	yawing moment coefficient ($\sim$)		β	sideslip angle (deg)
C_F	skin friction coefficient ($\sim$)		γ	heat capacity ratio ($\sim$)
D	drag (N)		δ_{r}	rudder deflection (deg)
e	geometry coefficient ($\sim$)		ϵ	wing twist angle (deg)
f	form factor ($\sim$)		λ	wing taper ratio ($\sim$)
H	cabin geometry parameter (m)		Λ	leading-edge sweep angle (deg)
k	planform geometry coefficient ($\sim$)		ρ	air density at cruise condition (kg/m^3)
L	lift (N)			
M	Mach number ($\sim$)			

---

[*]Student, Faculty of Aerospace Engineering
[†]Assistant Professor, Faculty of Aerospace Engineering, r.vos@tudelft.nl, Senior Member AIAA
[‡]COO ParaPy B.V.
[§]CEO ParaPy B.V.

American Institute of Aeronautics and Astronautics

I.   Introduction

Over the last five decades, commercial aviation has been monopolised by the traditional tube-and-wing configuration, which features cylindrical fuselage, swept wing, rear empennage and engines podded under the wing. Many improvements in different disciplines, such as aerodynamics, propulsion, structure and avionics have been resulted in a 100% efficiency gain over airliners of 50 years ago.[1,2] Nevertheless, the Airbus A350 and Boeing 787 represents an asymptote in terms of overall efficiency. In addition, manufacturers have to cope with a considerable commercial aviation growth predicted for the next decades and the consequent constraints related to environmental impact, pollution and noise.[3] Hence, different innovative design configurations have been explored lately with the aim of reducing the fuel consumption per passenger. For instance, Bolsunovsky *et al.* claim that the flying wing (FW) concept represents a viable alternative to solve the problems above mentioned because different tasks, namely providing lift, trimming the aircraft and accommodating people, are fulfilled by a unique integrated component.[4] This entails a reduction in wetted area for the same payload. Also Martinez-Val *et al.*[5] highlight the possible operational benefits of a 300-seat FW: a range factor improvement of 15-20% is claimed to be possible with the FW introduction.

Even though flying wings have been a topic of research and development for more than a century, they are still considered as novel configurations. The dominant reason for the slow acceptance of these vehicles is related to stability and control issues, which limit the mission to the cruise one,[6] structural penalty due to pressurization stresses in non-cylindrical cabins, emergency evacuation design and passenger acceptance. On the other hand, many researchers point out remarkable aerodynamic and structural advantages due to the low wetted area and interference drag, and beneficial spanwise weight distribution.[2] Moreover, the noise produced by the engines mounted over the trailing edge is shielded by the wing. The first projects on tailless aircraft date back to the 1930s with Lippisch and Horten and 1940s when Northrop worked on the prototypes of the YB-49.[7] Lately, researchers have been working on two different tailless aircraft configurations: pure FWs,[1,3,4,7–12] characterized by straight leading and trailing edge, and BWBs,[13–18] which feature a smoothly blending of the wing into the body.

The aerodynamic design philosophy applicable to unconventional configurations is not straightforward due to the non-consolidated knowledge and experience.[9] Therefore, high-fidelity design optimization is performed from the initial phases. Qin et al.[15,16] implement a three steps approach within the MOB project on a BWB, involving optimization. They use a full potential solution coupled with a boundary layer solution, and then Euler. Mialon et al.,[9] at ONERA, design the flying wing by manually exploring the design space and, then, setting up a systematic optimization. An Euler solver coupled with boundary layer equations is adopted. Li et al.[19] implement a multi fidelity procedure: they explore the design space with the aid of low fidelity codes in order to filter out non-satisfactory design points. Then a Reynolds-averaged Navier-Stokes (RANS) solver is used for a CFD-driven optimization. Aerodynamic shape optimization with high fidelity tools is also applied by Reist and Zingg[18] to investigate the BWB configuration and Mader[12] to find the optimum flying wing design. The former use RANS equations whereas the latter adopts Euler equations to capture transonic flow phenomena.

A new FW concept has been conceived and studied by Benad[20,21] at Technishe Universitat Berlin in collaboration with the Future Project Office at Airbus GmbH (Hamburg, Germany). The result of the conceptual study is named Flying V Wing due to the characteristic V-shaped planform (see Figure 1). It features trailing-edge elevons for longitudinal and lateral control, tip-mounted twin fins with rudders to fulfil directional stability and control functions, respectively. Two turbofan engines are placed over the wing trailing edge. Unlike the usual pressurized cabin configuration of blended-wing-body (BWB) aircraft and pure FW aircraft, the proposed Flying V is designed to have two cylindrical components, one in each wing half: this arrangement is structurally beneficial to bear pressurization loads.[22] Due to the high wing sweep the two legs of the V, the the streamwise cross-section of the cylindrical section results in an ellipse. This entails an efficient use of the volume of the wing without a large structural penalty due to the cylindrical nature of the cabin. In terms of top level requirements, the objective of this innovative concept is an aircraft with the highest lift-to-drag ratio and lowest structural mass such that is competitive with a state-of-the-art commercial aircraft, such as the A350-900. This implies a nominal range of 14,350 km, a service ceiling of 13,100 m, a cruise Mach number of 0.85, and a passenger capacity of 440 passengers [a].

The Flying V design is at a conceptual stage: the aircraft weight is estimated by handbook methods,

---

[a]Dimensions & key data — airbus, a leading aircraft manufacturer.   Retrieved on March 12th, 2016 from http://www.airbus.com/aircraftfamilies/passengeraircraft/a350xwbfamily/a350-900/specifications/
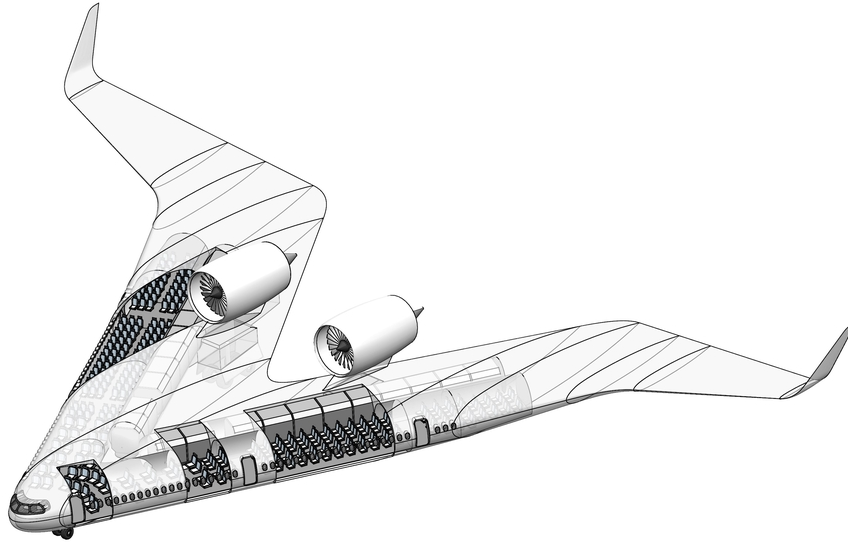
American Institute of Aeronautics and Astronautics

Figure 1. Flying V 3D geometry resulting from the conceptual study[20]

whereas drag is evaluated by vortex lattice methods and empirical correlations. The concept looks considerably promising: satisfactory gains in terms of drag and weight are estimated, which entail a 10% increase in lift to drag ratio compared to the A350-900.[20] The question is, does the Flying V concept indeed have these aerodynamic advantages, as predicted by the preliminary assessment? Therefore, the goal of the presented study is to perform the aerodynamic design process of the Flying V and assess the aerodynamic performance in cruise conditions. Since no aerodynamic data on the A350-900 data is available for comparison, the NASA Common Research Model (CRM)[23] is adopted as a benchmark for a modern commercial passenger aircraft of this class. In order to answer the central question, it is required to address a number of subquestions, i.e: how can the Flying V three-dimensional geometry be parametrized, and what is the most suitable aerodynamic analysis method for this application?

The present work focuses on aerodynamic characteristics during cruise conditions. Therefore, low-speed performance, field performance, and maximum lift coefficient will need to be addressed by future studies. The paper is laid out as follows. First the proposed aerodynamic design procedures are presented in Section II. Then, in Section III the chosen aerodynamic analysis method is compared to experimental data to demonstrate its validity. In Section IV four aerodynamic designs of the Flying V are presented and their aerodynamic performance is discussed and compared to the NASA CRM. Finally, conclusions of this study are presented (Section V) and recommendations for future studies are made.

II.   Flying V Design Procedure and Methodology

The Flying V design method is implemented in ParaPy. ParaPy is a Knowledge Based Engineering (KBE) environment[b]. It is selected due to the capability of automating repetitive tasks in a fast, efficient and demand-driven way. In particular, it allows for automatic geometry and grid generation, coupling with analysis tools, and support for multidisciplinary design optimization (MDO). The core of the program is the multi model generator (MMG), which creates the Flying V geometry according to a limited set of input parameters. Then, the aircraft geometry is fed into different analysis and sizing modules: the aerodynamic discipline is the focus of this investigation, whereas the structural sizing is concurrently performed in second study. Two additional modules are built in order to create a top-level design structure: the *performance analysis module*, which provides an estimation of the required fuel weight for a certain mission, aerodynamic efficiency, and weight and the *payload capacity module*, which calculates the amount of passengers that can be accommodated in the cabin. The top-level structure of the Flying V design application is shown in Figure 2.

The design strategy is outlined in Section A. Subsequently, the MMG, its structure and parametrization

---

[b]ParaPy. Retrieved on September 15th, 2016, from https://www.parapy.nl/

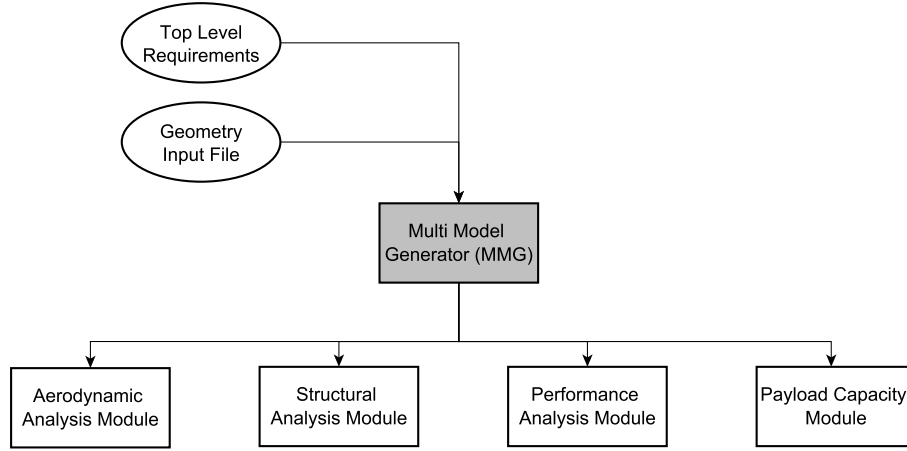American Institute of Aeronautics and Astronautics

Figure 2. Flying V design application top level structure

are presented in Section B, the aerodynamic analysis method is explained in Section C, and finally the performance and payload capacity classes are introduced in Section D and Section E, respectively.

A. Aerodynamic Design Strategy

As stated in Section I, shape optimization is used from the initial stages of the design of unconventional aircraft. The design approach for the Flying V is divided into wing design and twin-fins design, which are treated separately.

The wing design strategy chosen for the Flying V follows the stepwise procedure depicted in Figure 3. Initially, multi-fidelity design space exploration is applied to the *Baseline Configuration* (0) resulting in the *Improved Baseline Configuraiton* (1). Then, two different design approaches are followed: a dual-step optimization, which consists of planform optimization (2) and, subsequently, airfoil optimization (3), and single step optimization, where planform and airfoil variables are simultaneously varied (4).

The design space exploration (left-hand side of Figure 4) is used to efficiently move towards the optimal configuration: AVL is used to explore the design space, and the SU2 Euler solver to confirm the AVL results once they are deemed satisfactory. This is a manual procedure, which converges when further improvement cannot be manually achieved. On the other hand, the optimization procedures for maximum lift to drag ratio (or minimum cruise drag) are automatic and coordinated by the Differential Evolution (DE) algorithm, developed by Storn and Price.[24] It is a direct search algorithm capable of finding the global minimum of a multivariate function. The main features that make it suited for this type of application are: robustness and capability of handling non differentiable and highly non linear cost functions, suitability for parallel computing, ease of use, and good convergence properties. In mathematical notation, the optimization problem can be expressed as:

$$
\begin{aligned}
\min_{\bar{y} \in R^n} \quad & -L/D(\bar{y}) \\
\text{s.t.} \quad & \bar{g}(\bar{y}) \leq 0
\end{aligned}
\tag{1}
$$

The design vector $\bar{y}$ and inequality constraints $\bar{g}(\bar{y})$ of each design step are reported in Table 5 of Section IV.

The twin fins design procedure is applied to the Flying V resulting from the dual step and single step optimization procedures (Figure 3). The vertical tail should fulfill the following requirements:[25] positive directional static stability in all conditions, balance in a one-engine-inoperative (OEI) condition at take-off, and balance under maximum crosswind in landing configuration. In case these requirements (summarized in Table 1) are not met, the vertical surface area is increased or the planform parameters are changed. The candidate fin is the smallest one which satisfies the driving requirements. Hence, the cost function of the problem is the fin area, the constraints are represented by the requirements, and the design variables are
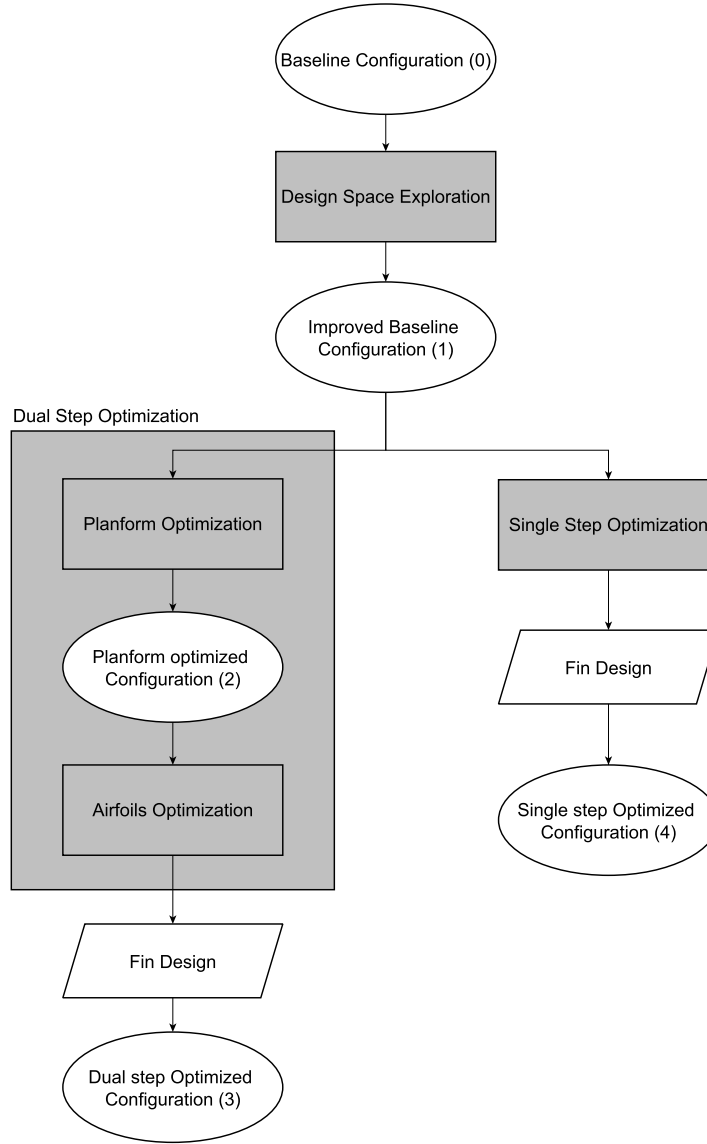
American Institute of Aeronautics and Astronautics

Figure 3. Flying V design strategy: top level structure

aspect ratio, leading edge sweep angle and taper ratio. In mathematical notation:

$$
\begin{aligned}
\min \quad & S_{\text{fin}}(\Lambda_{\text{fin}}, A_{\text{fin}}, \lambda_{\text{fin}}) \\
\text{s.t.} \quad & C_{n_\beta} \geq 0 \\
& \delta_{\text{r}}^{\text{OEI}} \leq 20° \\
& \delta_{\text{r}}^{\text{CW}} \leq 20°
\end{aligned}
\tag{2}
$$

The required δ_r and the $C_{n_{\beta_v}}$ are computed by empirical correlations,[26] whereas the yawing moment derivative in tail-off condition is evaluated by SU2. Moreover, the rudder is assumed to be full span and the chord ratio is 0.3. Since it is a pure aerodynamic optimization, tight bounds on the variables are required to prevent a high sweep angle and low taper ratio (they are outlined in Section IV). Again, the DE optimization algorithm is used.
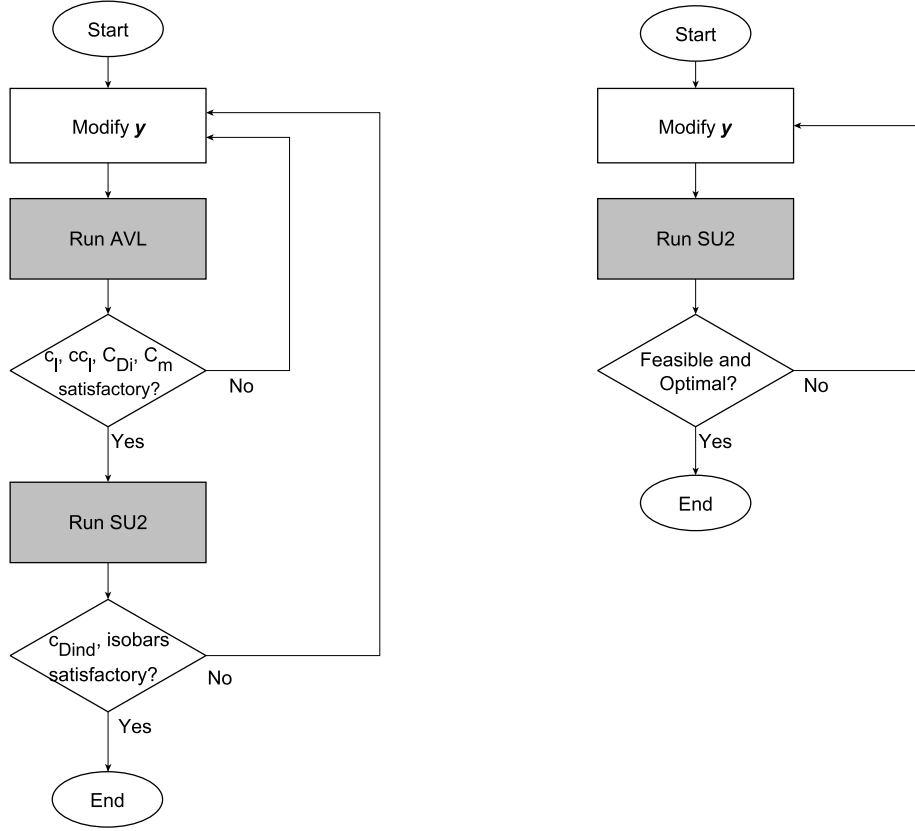
American Institute of Aeronautics and Astronautics

Figure 4. Flying V design strategy: multi-fidelity design space exploration (left) and optimization procedure (right).

Table 1. Twin fins driving requirements

Requirement	Brief description	Criteria
Directional static stability	The yawing moment induced by the sideslip must push the aircraft back to the initial state	$C_{n_\beta} > 0$
OEI condition at take off	When one engine fails, the aircraft must be able to balance the asymmetric thrust ($\beta = 0°$)	$\delta_r < 20°$
Crosswind landing	An aircraft must be balanced during landing at 11.5° sideslip	$\delta_r < 20°$

B.   Multi Model Generator

The concept proposed by Benad[20] envisions a *single-shell* structure, which is able to carry pressurization stresses but also aerodynamic and inertial loads. In particular, a cylindrical passenger cabin is placed in the wing's leading edge and an additional cabin compartment is located behind it. Even though this layout is optimal for structural reasons, it does not allow for enough design flexibility. As an alternative, the oval cross section proposed by Vos *et al.*[27] represents a viable solution. The oval section provides more design flexibility than its cylindrical counterpart: it is defined by 4 variables rather than 1. Moreover, by placing the cabin shells parallel to the highly-swept leading edge, the vertical cabin cross-section in the streamwise direction (i.e. in the xz-plane) resembles a stretched ellipse. Therefore, this solution proves to be volume efficient. The two streamise profiles with the integrated cabin shells are shown in Figure 5.

The proposed cabin configuration is shown in Figure 6 (blue): the oval cross sections are perpendicular to the leading edge (from sections 3 to 4) until a certain point, called *transition point* (TP), where they
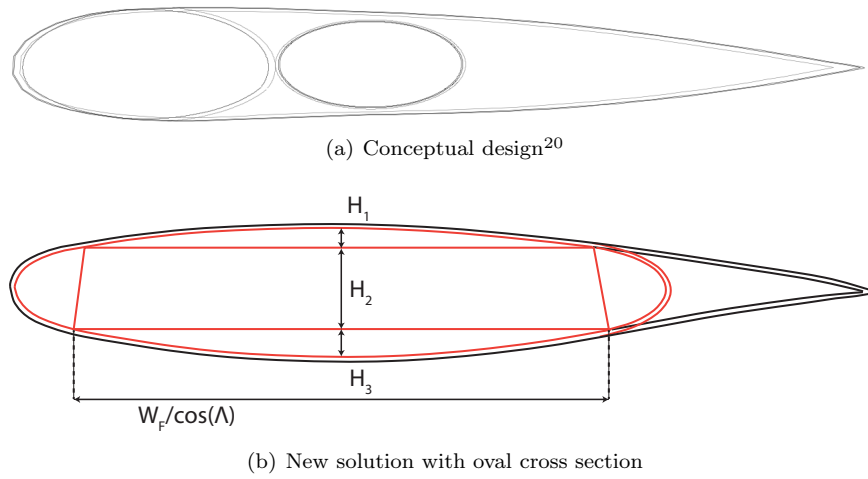
(a) Conceptual design[20]

(b) New solution with oval cross section

Figure 5. Streamwise profile with integrated cabin

become perpendicular to the flight direction (the way Vos *et al.*[27] originally envisioned the concept). This means that, in the nose cone (from sections 1 to 2), the wide oval cabin is symmetric in the xy-plane. Hence, there exists a transition region (from sections 2 to 3) in which the oval cross sections rotate. The fuselage segment between sections 4 and 5 is strongly tapers. Here, the pressurized fuselage is formed by an inner shell, while a second, non-pressurized shell forms the outer skin.
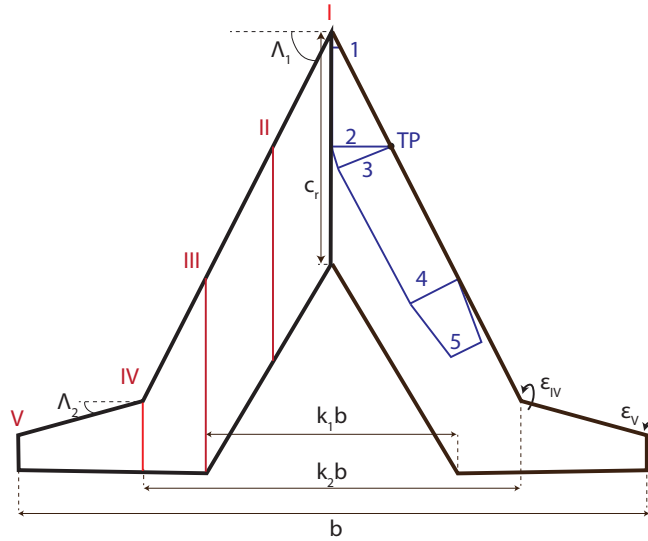
Figure 6. Flying V top view: streamwise profile sections on the left and cabin sections on the right

In terms of outer mold line parametrization, 10 planform design variables are defined to control the planform shape of the aircraft: surface area, span, root chord, overall taper ratio, 2 leading edge sweep angles, 2 relative kink locations, and 2 twist angles of profile sections IV and V (see Figure 6). Then, regarding the cross sections, the inboard part (where the passengers are allocated) is cabin driven, whereas the outboard region (between sections IV and V) is similar to the wing of a conventional wide-body aircraft. The cross-sectional variables are displayed in Figure 7. Each oval cross section is defined by 4 parameters. As shown in Table 2, some parameters are fixed according to top level requirements and design choices, others are mutually dependent. Hence, 6 oval sections parameters are free to vary: H_1 and H_3 of sections 2,3 and 4 (Figure 7).

American Institute of Aeronautics and Astronautics

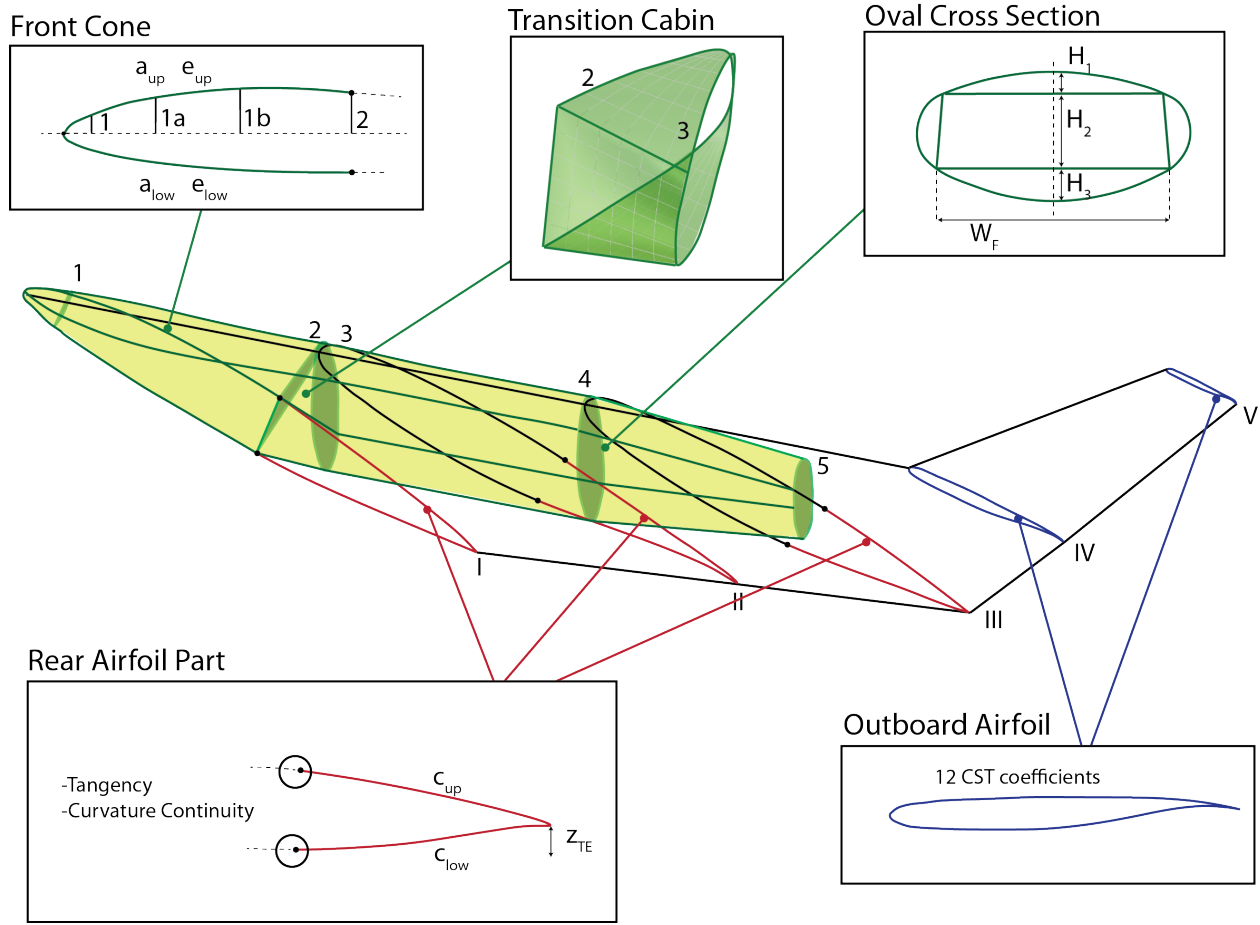**Figure 7. Flying V outer mold line parametrization**

Table 2. Oval cross sections parameters: fixed values

Oval cross section	Variable	Value	Explanation
1	H_1 (m)	dependent	Based on nose cone parametrization (a_{up}, e_{up})
	H_2 (m)	1.2	Minimum height where cockpit starts
	H_3 (m)	dependent	Based on nose cone parametrization (a_{low}, e_{low})
	W_F (m)	dependent	Determined by H1, H2, H3 and total oval width
2	H_2 (m)	2.1	Top level requirements
	W_F (m)	dependent	Determined by H1, H2, H3 and total oval width
3	H_2 (m)	2.1	Top level requirements
	W_F (m)	6	Design choice to have 10 people rows
4	H_2 (m)	2.1	Top level requirements
	W_F (m)	6	Design choice to have 10 people rows

The cabin region between sections 1 and 2 is parametrized by 4 cone variables, which define profile I, whose upper and lower curves are polynomials of type:

$$z(x) = a\sqrt{x} + dx^2 + ex^3 + b \tag{3}$$

In which the parabolic term $a\sqrt{x}$ is included to guarantee the tangency of the two curves at the leading edge. Then, each curve is imposed to pass through two points, namely the most forward point of the aircraft and

the upper (and lower) point of section 2 (Figure 7). Therefore, two degrees of freedom allow the tailoring of each curve (a_{low}, e_{low} and a_{up}, e_{up}, see Figure 7). Then, profile sections I, II, and III of Figure 6 are created by intersecting 3 planes with the generated cabin and then attaching a rear airfoil part (or fairing). Each rear airfoil part is defined by a lower and upper 4th order polynomial of type:

$$z(x) = ax^4 + bx^3 + cx^2 + dx + e \tag{4}$$

By imposing tangency and curvature continuity, each rear airfoil part has 3 degrees of freedom in total (c_{up}, c_{low}, z_{TE}, see Figure 7). Hence, the rear fairings of profiles I, II and III are defined by 9 variables. On the other hand, profiles IV and V are defined by 12 Class-Shape-Transformation (CST) variables[28] each. The winglet is defined by 3 parameters: taper ratio, aspect ratio and leading edge sweep angle. Hence, the total number of design parameters is 56: they are grouped in different vectors, as reported in Table 3.

Table 3. Design variables grouped in design vectors

Vector	Variables	Number
$\bar{y}_{\mathrm{planf}}$	S, b, c_{r}, Λ_1, Λ_2, λ, k_1, k_2, ϵ_{IV}, ϵ_{V}	10
$\bar{y}_{\mathrm{oval}}$	H_{1_2}, H_{3_2}, H_{1_3}, H_{3_3}, H_{1_4}, H_{3_4}	6
$\bar{y}_{\mathrm{nose}}$	a_{up}, e_{up}, a_{low}, e_{low}	4
$\bar{y}_{\mathrm{rear}}$	$c_{\mathrm{up_I}}$, $c_{\mathrm{low_I}}$, $z_{\mathrm{TE_I}}$, $c_{\mathrm{up_{II}}}$, $c_{\mathrm{low_{II}}}$, $z_{\mathrm{TE_{II}}}$, $c_{\mathrm{up_{III}}}$, $c_{\mathrm{low_{III}}}$, $z_{\mathrm{TE_{III}}}$	9
$\bar{y}_{\mathrm{CST}}$	$CST_{i_{\mathrm{IV}}}$ for i = 1,2,...,12, $CST_{i_{\mathrm{V}}}$ for i = 1,2,...,12	24
$\bar{y}_{\mathrm{fin}}$	A_{fin}, λ_{fin}, Λ_{fin}	3

The engines of the reference aircraft, the Trent XWB 84, are considered. Furthermore, a preliminary shape of the pylon is determined to account for the wetted area increase to estimate its impact on profile drag. The control surfaces are not included in the MMG at this stage. An example of the Flying V complete geometry created by the MMG is displayed in Figure 8.
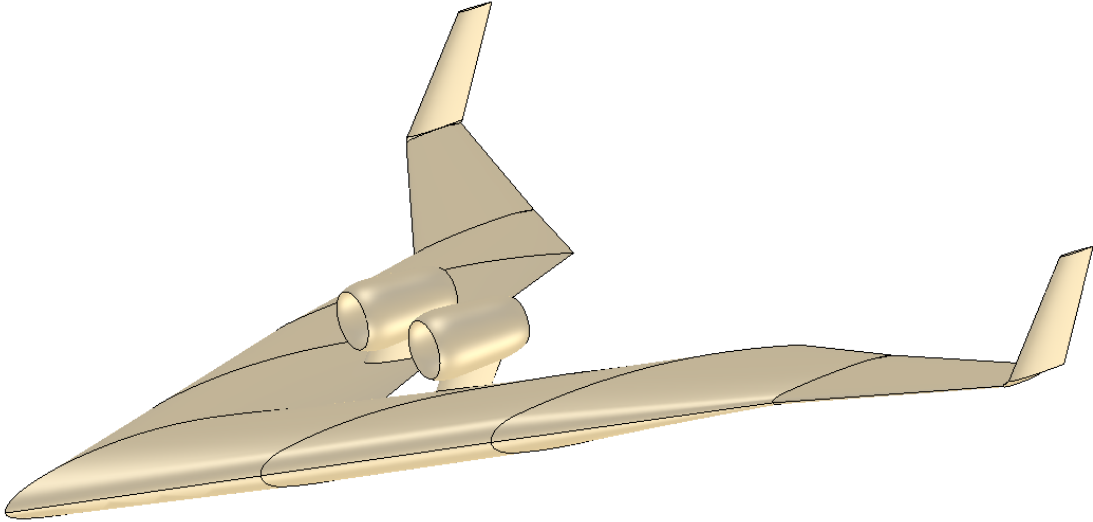
Figure 8. Flying V 3D model generated by the MMG.

C.   Aerodynamic Analysis Module

The *aerodynamic analysis module* features three sub modules as shown in Figure 9. The Euler flow model is selected for the three-dimensional aerodynamic analysis because of the capability of predicting the pressure distribution in transonic conditions, including the formation of shock waves. The numerical implementation of the Euler equations has a relatively low computational cost compared to the RANS equations but lacks

American Institute of Aeronautics and Astronautics

viscous or heat-transfer effects. The Stanford University Unstructured suite (SU2) is chosen. This is an open-source package of C++ software tools designed with Computational Fluid Dynamics (CFD) and aerodynamic shape optimization in mind.[29]
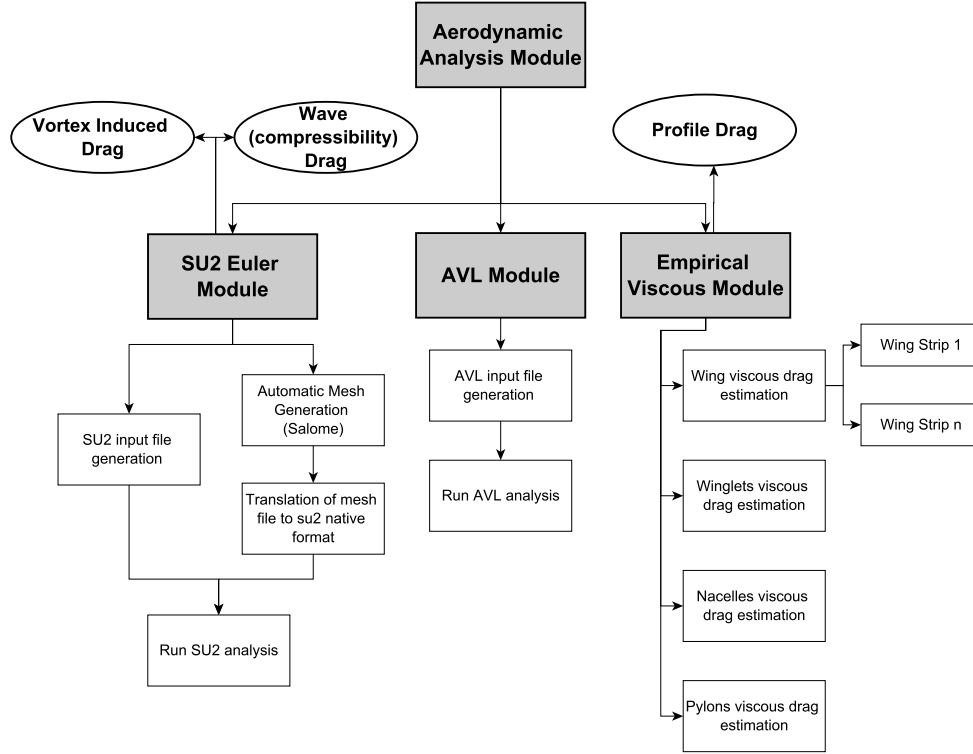

Figure 9. Aerodynamic analysis module

The *SU2 Euler module*, implemented in ParaPy, generates the configuration file for the solver, which contains a set of user's options, such as flight conditions, reference system, numerical solver and convergence criteria. In addition, it produces the unstructured mesh invoking the Salome package in ParaPy. Subsequently, it translates the grid file into the native format required by the SU2 suite. Then, it runs the solver, extracts the aerodynamic coefficients, and plots the pressure distributions at different spanwise locations. Since the Euler flow model neglects viscosity, it is able to estimate the inviscid drag components (vortex induced drag and wave drag), which are grouped in C_{D_inv}. Hence, a separate *empirical viscous module* is created to compute the Flying V profile drag (Figure 9). In particular, the profile drag is made up by three contributions: skin friction, pressure, and lift-related profile drag. As explained by Gur et al.,[30] the third contribution can be neglected since the analysis focuses on cruise condition: this assumption is further confirmed in Section C. The remaining two components are addressed simultaneously with the following formulation:

$$C_{D0} = C_F \cdot f \cdot \frac{S_\text{wet}}{S} \tag{5}$$

Where C_F is the flat-plate skin-friction coefficient, f is the form factor of each component, which accounts for pressure drag due to viscous separation (valid until drag divergence[31]), S is the reference area, and S_{wet} is the wetted area. The Flying V is separated into the following components: wing, winglets, nacelles and pylons and Eq. 5 is applied to each of them. The form factor and flat plate skin friction coefficient of each component are computed by semi-empirical equations.[31] The Flying V lift-to-drag ratio can be calculated as:

$$\frac{C_L}{C_D} = \frac{C_L}{C_{D0} + C_{D_\text{inv}}} \tag{6}$$

Finally, the *AVL module* generates the input file required by AVL, runs the program and produces the lift and moment distribution at a low computational cost.

American Institute of Aeronautics and Astronautics

The tetrahedral unstructured grid is generated by the Salome meshing tool embedded in ParaPy, starting from the 3D geometry. An example of a coarse grid is shown in Figure 10 on the right hand side. The generation follows the called bottom-up flow: nodes on vertices are created first, then edges are split into segments and the surface and volume meshes are created. This automatically guarantees the conformity of the mesh. Moreover, meshed surfaces are assembled in groups in order to assign boundary conditions (see Figure 10): an Euler boundary condition on the wing, a far-field condition on the computational domain boundaries, and a symmetry condition on the symmetry plane. The computational domain used for the numerical analysis is a large parallelepiped and the far-field boundary is located around 20 body lengths away from the airplane (Figure 10), as suggested by Chan et al.[32] Regions characterized by higher curvature, like the wing leading edge and trailing edge have a higher grid refinement. Close to leading edge, the element size of the surface grid is ∼0.1% of the local chord length.
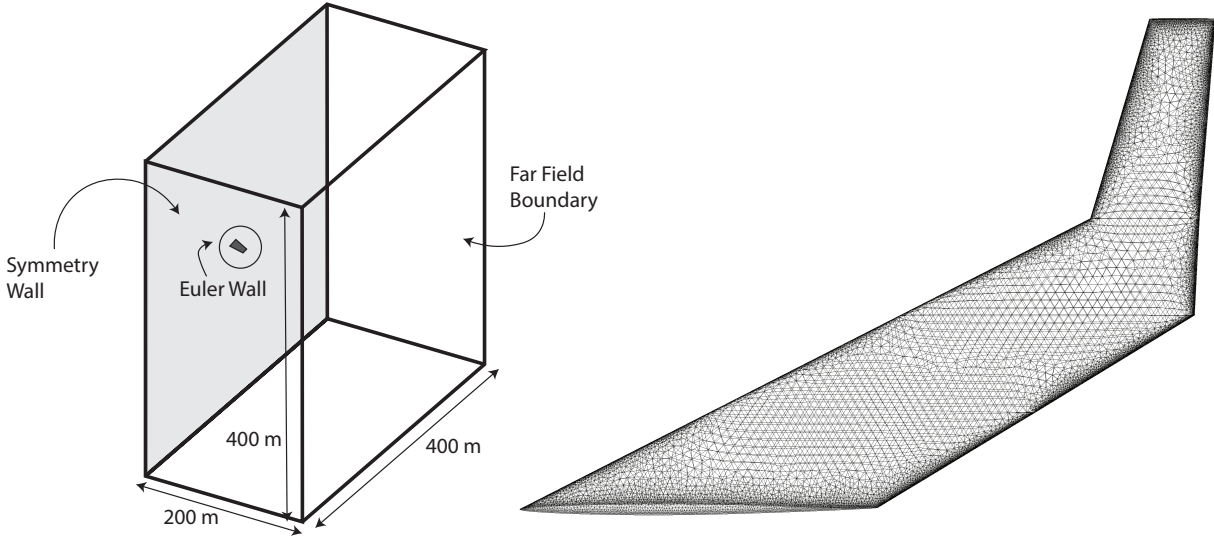

Figure 10. Grid computational domain with dimensions and boundaries (left) and example of grid generated by ParaPy (right)

D. Performance Analysis

The performance analysis module estimates the fuel weight required to complete the flight mission. The *Fuel Fraction Method* as presented by Roskam[33] is used, i.e. the fuel weight required for cruise is evaluated using the Breguet range equation, whereas the contributions of other segments are calculated with statistical factors.

E. Payload Capacity

The payload capacity module provides a preliminary estimation of the amount of passengers that can be accommodated in the Flying V. The objective is to match the maximum capacity of the reference aircraft, i.e 440 passengers in economy class. The required total freight volume is 172.4 m^3. The required galley and lavatory space is estimated with empirical correlations suggested by Raymer,[31] whereas the cockpit area is estimated with the statistical factors outlined by Torenbeek.[22] The total floor area dedicated to payload is extracted from the geometry model implemented in ParaPy; by subtracting the aforementioned areas from the total area, the floor area available to accommodate passengers is computed. The maximum passenger capacity is computed considering a twin-aisle cabin with 10 passengers per row, measuring 6m width and a 0.81m seat pitch.[20] The passenger capacity (n_{pax}) represents a constraint in the design optimization, as outlined in Section IV.

American Institute of Aeronautics and Astronautics

III. Validation and Verification

In this section, a grid converged study and quality assessment are outlined. Subsequently, the validation and verification of the aerodynamic solver are presented.

A. Grid Convergence Study

A grid convergence analysis is performed in order to determine the coarsest mesh which guarantees acceptable results. In particular, for aerodynamic shape optimization, in which the computational time of a single simulation plays a relevant role, it is more important that the aerodynamic phenomena are captured rather than the exact coefficients are estimated. The results of the convergence test are shown in Figure 11. The error is relative to the value of the finest tested grid. The results obtained with around 1 million cells are deemed accurate enough for the shape optimization purpose, because the drag and pitching moment coefficients are within the 1% and 3% error respectively.
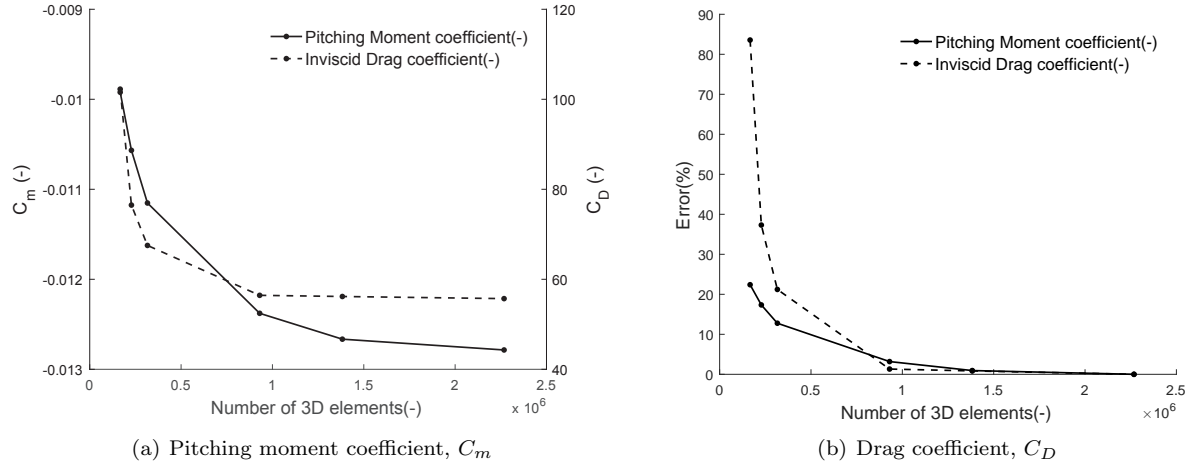

(a) Pitching moment coefficient, C_m (b) Drag coefficient, C_D

Figure 11. SU2 grid convergence study for Flying V aircraft at $M = 0.85$ and $C_L = 0.26$.

B. Grid Quality Assessment

In order to estimate the quality of the grid automatically generated by ParaPy, the Flying V baseline configuration is meshed in ICEM CFD, which has multiple options to locally change refinement and incorporates advanced smoothing algorithms. The resulting ICEM CFD mesh has similar size and refinement. Then, the two grids are compared with each other within ICEM CFD based on the 3 criteria: dihedral angle, aspect ratio and equiangle skewness. According to Woodard et al.,[34] the dihedral and aspect ratio are quality measures which apply to individual elements, whereas the equiangle skewness accounts for the interaction with the surrounding elements. The dihedral should not be close to 0° and 180°. The aspect ratio is calculated as the ratio between the volume of the element and the radius of the circumscribed sphere to the third power, then normalized with the equilateral tetrahedron:

$$\text{Aspect Ratio} = \frac{(V/r^3)_{\text{actual}}}{(V/r^3)_{\text{ideal}}} \tag{7}$$

This means that the value should be as close as possible to 1. The equiangular skewness, on the other hand, is a measure of the distortion of surrounding cells: this parameter should not be lower than 0.1 in case of tetrahedrons.

The results of the comparison are presented in Figures 12(a) to 12(c). The dihedral angle (see Figure 12(a)) of both the grids satisfies the upper and lower bounds of 170° and 10°. In terms of aspect ratio (see Figure 12(b)), the ICEM grid has 20% of elements with values higher than 0.9 and the others spread in a uniform way from 0.4 to 0.9; there are very few elements with a low aspect ratio. On the other hand, the aspect ratio of the ParaPy grid shows a distribution similar to a Gaussian one: the majority of the elements
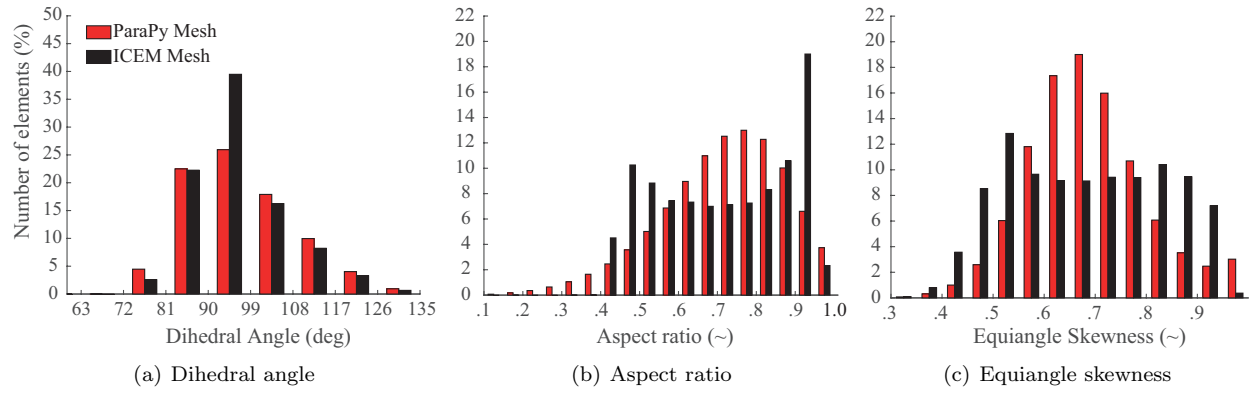
American Institute of Aeronautics and Astronautics

(a) Dihedral angle   (b) Aspect ratio   (c) Equiangle skewness

Figure 12. Comparison between ParaPy-Salome-generated grids and ICEM-generated grids

is between 0.6 and 0.9, but there are some elements with values lower than 0.4. In a nutshell, even though the mean value (0.717 for the ICEM mesh and 0.714 for the ParaPy one) is almost the same, the ICEM grid has a higher quality in terms of aspect ratio due to a lower number of elements with a low value. Similar trends are depicted in Figure 12(c), in case of the equiangle skewness. However, elements with prohibitively low values are neither present in the ICEM nor in the ParaPy grid. The mean value is 0.679 and 0.687 for the ICEM and ParaPy grids respectively, hence the latter performs slightly better according to this quality measure. In conclusion, the quality of the ParaPy mesh is deemed satisfactory since it is comparable in quality to a mesh produced by a more sophisticated program.

C.   SU2 Validation and Verification

The aerodynamic solver outlined in Section C is validated with the experimental results of the Onera M6 wing. The simulation uses the flow conditions of Test 2308 reported by Schmitt and Charpin:[35] Mach number equal to 0.8395, angle of attack of 3.06° and Reynolds number of $11.72 \cdot 10^6$. The computational domain of the SU2 Euler implementation is a large parallelepiped. The mesh is characterised by 140,244 tetrahedral elements. Different numerical methods to solve the convective flow equations are tested: the Jameson Schmidt Turkel (JST) scheme proves to be really stable and reaches convergence faster, while the Roe solver is more accurate with the same mesh refinement. The pressure distributions resulting from the numerical analysis are compared to the experimental data at two spanwise loctions and shown in Figure 13(a) and Figure 13(b), respectively. The overall agreement is satisfactory since the trends are captured well by the Euler analysis: the strong shock wave in the outer part is accurately predicted.
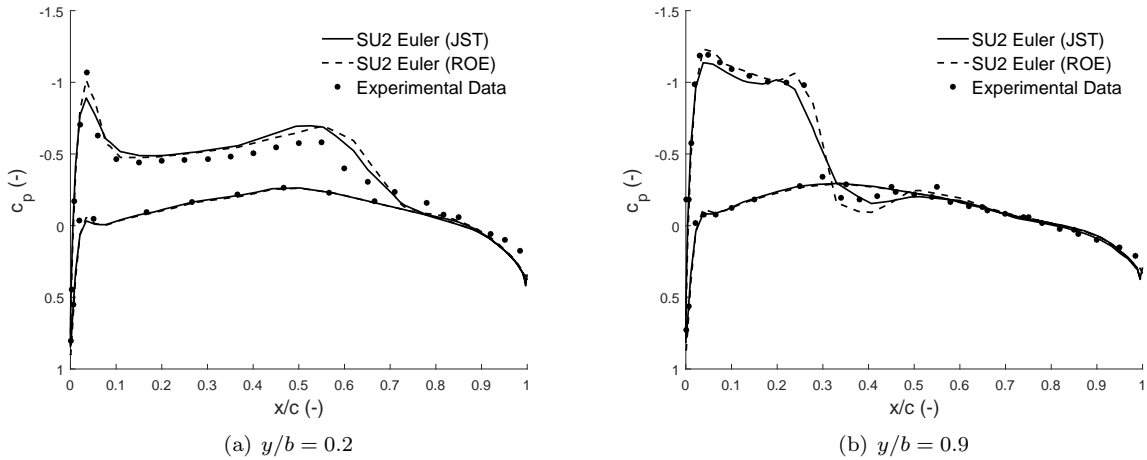

(a) $y/b = 0.2$ (b) $y/b = 0.9$

Figure 13. Pressure distribution over ONERA M6 wing

American Institute of Aeronautics and Astronautics

Furthermore, it is important to compare the aerodynamic coefficients, which drive the aerodynamic design and shape optimization. Since the experimental data does not include coefficients, the results obtained from SU2 Euler are compared to other studies involving RANS, Delayed Detached Eddy Simulation (DDES) and Detached Eddy Simulation (DES), as previously done by Durrani and Qin.[36] This represents the verification process. Furthermore, RANS simulations are performed with SU2 in order to compare the Euler results at different angle of attacks with a higher order code. The profile drag coefficient is added to the inviscid drag coefficient computed by Euler. The wing form factor outlined by Torenbeek is used since it compares well with the RANS calculations and previous studies. The drag polar is shown in Figure 14. The results coming from the JST numerical method show a really good agreement with the RANS outcome; moreover, the curve fits perfectly between the points generated by other investigations with RANS, DES and DDES, represented with star markers. The Roe method results have a small offset at low lift coefficients and then they converge to the JST ones. Besides, the assumption of neglecting the additional 2D profile drag at low lift coefficients is further confirmed by this verification.
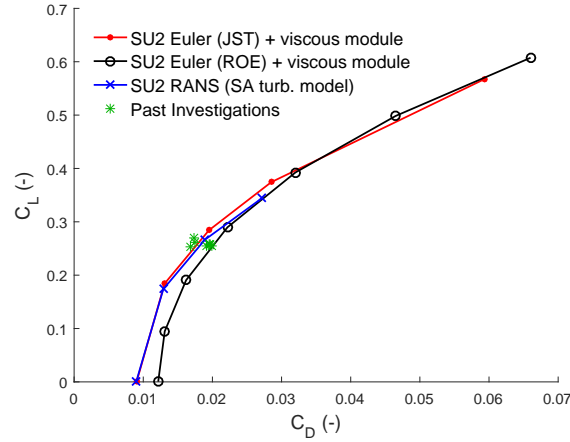

Figure 14. Onera M6 drag polar (M=0.8395). Past investigations reported by Durrani and Qin[36]

In addition, further verification is obtained by comparing the drag coefficient of the NASA CRM with open literature results. This configuration aims to reproduce the geometry of a modern, long-range commercial airplane operating at transonic flight conditions ($M = 0.85$) and is adopted as a benchmark for validation purposes.[23] In the CRM model, the advanced supercritical wing is attached to a Boeing 777-200ER fuselage geometry, which has a passenger capacity similar to the A350-900 and a similar range. The study performed by Ueno et al.[37] is chosen as a benchmark: it is a far-field drag analysis of the NASA CRM (wing, body and horizontal tail) based on the CFD simulations performed by JAXA for the fourth AIAA drag-prediction workshop. The total drag counts resulting from the far-field analysis are 268 (slightly lower than 271, computed by JAXA). The drag coefficient resulting from the analysis method outlined in Section C is equal to 252 counts. These estimations are within a 6% difference, hence the agreement proves to be satisfactory.

IV.   Results and Discussion

The aerodynamic design of the Flying V is optimized for a single condition, i.e. the cruise condition. The cruise weight assessed during the preliminary assessment[20] is equal to 200,000kgf. The nominal cruise lift coefficient can be defined according to cruise weight, Mach number, nominal altitude and reference area (equal to the wing planform area), considering ISA conditions:

$$C_{L_{\text{cruise}}} = \frac{2W_{\text{cruise}}}{p_{\text{cruise}}\gamma M_{\text{cruise}}^2 S} \qquad (8)$$

The cruise Mach number is equal to 0.85 and the design altitude is chosen to be 13,000 m, slightly lower than the service ceiling (13,100 m) of the reference aircraft. The cruise design conditions are summarized in Table 4. It is relevant to remark that the SU2 is run with a fixed lift coefficient as input.

American Institute of Aeronautics and Astronautics

Table 4. Flying V design conditions

Parameter (unit)	Value
Mach ($\sim$)	0.85
C_{L_cruise} ($\sim$)	0.26
p_cruise (Pa)	16510.38
ρ_cruise (kg/m^3)	0.27
T_cruise (K)	216.65

Since a weight estimation and center-of-gravity estimation is not included in this study, an assumption is made in order to estimate the reference point for the pitching moment computation. Hence, for each Flying V planform, the neutral point is computed with AVL, and the center of gravity is placed ahead of it in order to guarantee longitudinal static stability. A typical transport aircraft usually have a static margin (distance between neutral point and center of gravity) of 5% of the mean aerodynamic chord (MAC) at the most-aft centre of gravity position.[31] However, since the MAC of the Flying V is twice as much the reference aircraft one, a static margin of 2.5% is chosen in order to arrive at a comparable absolute distance. Hence, the center of gravity is assumed to be 6% MAC ahead of the neutral point at the design condition. This distance is around 1m for the baseline configuration and is assumed to be an average between the most forward and aft possible center of gravity locations.

The Flying V baseline configuration is mainly deduced from the Airbus report[20] and the NASA/Langley Withcomb supercritical airfoil with thickness to chord ratio of 9% is selected for sections IV and V (Figure 6), due to satisfactory performance in the transonic regime.[38]

A. Test Case

The different design steps reported in Figure 3 are followed. The objectives, inequality constraints and design variables of each step are reported in Table 5. The DE algorithm requires the following inputs: the population size is set to 4 times the number of design variables and the maximum number iterations to 20. Each SU2 simulation is stopped after 100 iterations because the results in terms of aerodynamic coefficients are within a 0.5% deviation with respect to the converged solution: this helps saving computational time. Each run takes about 20 minutes to complete on a single machine with the following performances: Intel i7 2.4 GHz processor, 16 Gb RAM DDR3 1600 Mhz.

The results of the optimization process is reported in Table 6. Note, that the configuration numbering refers to (Figure 3) and that Configuration 0 is the baseline configuration. The CST parameters of section IV and V of each of the five configurations are separately reported in Table 7. Note that the CST variables of configurations 0, 1 and 2 are identical. With the data of Tables Table 6 and Table 7 in combination with the parametrization definition of Section IIB, the outer mold line of the Flying V can be fully extracted. The resulting aerodynamic properties of each of the configurations are reported in Table 8. In the following subsection, these summarizing results are further discussed.

B. Multi-fidelity Design Space Exploration: from Config. 0 to Config. 1

results of the five configurations in terms of lift and lift coefficient distribution are displayed in Figure 15(a) and Figure 15(b), respectively. In addition, the Mach contours are depicted in Figures 16(a) to 16(e). The baseline configuration (Config. 0), displayed in Figure 15(a) and Figure 15(b) (black line), features too much load outboard, which comes with three non-negligible drawbacks: high wave and lift-induced drag, strong pitching moment (see Table 8) and large supersonic region ahead of the shock wave (Figure 16(a)). The maximum Mach number is 1.47: this may cause boundary layer induced separation, which cannot be predicted by an Euler solver.[39]

As reported in Table 5, the aim of the design space exploration is to improve the spanwise load distribution (reduce the induced drag and pitch down moment), reduce the supersonic region over the outboard wing surface and align the isobars close to the root. The first goal can be achieved by modifying the spanwise twist distribution and thickness; the second one can be attained by sweeping the outboard wing back and changing the taper ratio. Finally, the third goal can be obtained by moving the root-profile thickest point

American Institute of Aeronautics and Astronautics

Design Step	Objective(s)	Constraints	Design Variables
Design Space Explor.	Reduce induced drag Reduce pitch down Reduce supersonic flow Improve isobars	-	Λ_2, λ, ϵ_{IV}, ϵ_{V}, $\bar{y}_{\text{oval}}$, $\bar{y}_{\text{nose}}$, $\bar{y}_{\text{rear}}$
Dual step Planf. Optim.	$\min -L/D$	$C_m \geq -0.015$ $\alpha \leq 3°$ $n_{\text{pax}} \geq 440$	$\bar{y}_{\text{planf}}$
Dual step Airfoil Optim.	$\min -L/D$	$C_m \geq -0.010$ $\alpha \leq 3°$ $n_{\text{pax}} \geq 440$ $(t/c)_{\text{IV,V}} \geq 0.085$	$\bar{y}_{\text{CST}}$, ϵ_{IV}, ϵ_{V}, $\bar{y}_{\text{rear}}$
Single step Optim.	$\min -L/D$	$C_m \geq -0.015$ $\alpha \leq 3°$ $n_{\text{pax}} \geq 440$ $(t/c)_{\text{IV,V}} \geq 0.085$	$\bar{y}_{\text{planf}}$, $\bar{y}_{\text{CST}}$

further forward in order to shift the suction peak, and reducing the aft camber.[39] The value of the design variables after these modifications are reported in Table 5. The results of the improved-baseline configuration (Config. 1), are shown in Figure 15(a) and Figure 15(b) by the blue line. The inviscid drag is reduced from 71 to 56 drag counts (Table 8): this reduction is obtained by a more elliptical lift distribution, decrease in outboard local lift coefficient and maximum Mach number from 1.47 to 1.41 (Table 8). Also the size of the supersonic region greatly decreases (Figure 16(b)). This is a result of a large nose-down washout and increase in outboard sweep angle from 15° to 30° (Table 6). The pitching-moment coefficient is halved from -0.053 to -0.024, see Table 8. This improved baseline configuration already represents a big step forward. However additional improvements are investigated with automatic optimization procedures.

C.   Dual Step Optimization: from Config. 1 to Config. 3

The dual step optimization is one of the two approaches towards an optimum aerodynamic design (Figure 3). It features subsequent planform and airfoil optimization.

1.   SU2 Euler Planform Optimization: from Config. 1 to Config 2

The SU2 Euler planform optimization is applied to the improved baseline configuration (Config.1 in Figure 3). The design variables are the 10 planform shape parameters reported in Table 3: since the span is constrained to the 65m gate limit, the number of parameters decreases to 9. The constraints regarding angle of attack, pitching moment coefficient and passenger capacity are specified in Table 3. In addition, the DE algorithm requires lower and upper bounds for the variables, so that the elements of the population are chosen within the feasible design space: $\pm 20\%$ of the initial value is selected, except for the twist angles ($\pm 100\%$). The planform optimization procedure takes 33 hours in total. Two tricks are adopted to save computational time. Five simulations are simultaneously run by using parallel computing, and AVL is used to filter out non feasible design points when one of the following criteria is not satisfied: $C_m \geq -0.025$ and $\alpha \leq 4°$. A certain margin is used with respect to the actual constraints due to the relatively low accuracy of AVL.

In Figure 15(a), the lift distribution of the planform-optimized configuration (red line) is compared to the previous ones: the trend resembles an averaged elliptical/triangular distribution, which provides the best aerodynamic trade off, as proved by Qin et al.[15,16] This is mainly obtained by sweeping the outboard wing further back to 33.8°, reducing the taper ratio from 0.15 to 0.13 and increasing the nose-down wash out (Table 6). This last modification is responsible for the decrease in local lift coefficient over the outboard wing, as displayed in Figure 15(b). The peak local Mach number is lowered to 1.32 and the supersonic region

Table 6. Values of the design variables for five Flying V configurations. Note, that the configuration numbering refers to (Figure 3.

	Variable	Config. 0	Config. 1	Config. 2	Config. 3	Config. 4
Planform shape	S (m^2)	895.0	895.0	883.7	883.7	883.3
	b (m)	65.0	65.0	65.0	65.0	65.0
	c_r (m)	24.0	24.0	24.8	24.8	24.0
	$\Lambda_1(°)$	63.0	63.0	63.6	63.6	64.4
	$\Lambda_2(°)$	15.0	30.0	33.8	33.8	37.8
	k_1 ($\sim$)	0.400	0.380	0.385	0.385	0.386
	k_2 ($\sim$)	0.600	0.600	0.588	0.588	0.623
	λ ($\sim$)	0.18	0.15	0.13	0.13	0.13
	ϵ_{IV} (°)	-1.5	-4.0	-4.7	-4.3	-4.3
	ϵ_V (°)	-1.0	-3.0	-4.9	-5.0	4.4
Oval cross section 2	H_1 (m)	0.7	0.8	0.8	0.8	0.8
	H_3 (m)	0.5	0.6	0.6	0.6	0.6
Oval cross section 3	H_1 (m)	0.5	0.6	0.6	0.6	0.6
	H_3 (m)	0.7	0.7	0.7	0.7	0.7
Oval cross section 4	H_1 (m)	0.4	0.4	0.4	0.4	0.4
	H_3 (m)	0.7	0.7	0.7	0.7	0.7
Nose cone	a_{up} ($\sqrt{m}$)	0.8	0.9	0.9	0.9	0.9
	a_{low} ($\sqrt{m}$)	0.7	0.6	0.6	0.6	0.6
	e_{up} (1/m^2)	-2.5	-2.0	-2.0	-2.0	-2.0
	e_{low} (1/m^2)	-1.5	-1.0	-1.0	-1.0	-1.0
Rear Airfoil section I	c_{up} (10^{-3}/m)	-0.10	-0.08	-0.08	-0.05	-0.08
	c_{low} (10^{-3}/m)	-0.10	-0.08	-0.08	-0.07	-0.08
	z_{TE} (m)	-0.40	-0.55	-0.55	-0.50	-0.55
Rear Airfoil section II	c_{up} (10^{-3}/m)	-0.20	-0.10	-0.10	-0.11	-0.10
	c_{low} (10^{-3}/m)	0.10	0.10	0.10	0.15	0.10
	z_{TE} (m)	-0.100	-0.070	-0.070	-0.069	-0.070
Rear Airfoil section III	c_{up} (10^{-3}/m)	-0.100	-0.010	-0.010	-0.012	-0.010
	c_{low} (10^{-3}/m)	0.1	0.1	0.1	0.2	0.1
	z_{TE} (m)	-0.05	-0.05	-0.05	-0.04	-0.05

Table 7. CST variables of the five Flying V configurations. Configurations 1,2, and 3 have the same values

Config.-Sec.	$\bar{y}_{CST}$
0,1,2-IV	{0.1557, 0.0533, 0.1783, 0.0599, 0.1853, 0.2543, -0.1502, -0.1091, -0.0309, -0.3185, 0.0493, 0.2168}
3-IV	{0.1335, 0.0617, 0.2019, 0.0308, 0.1520, 0.2601, -0.0843, -0.0712, -0.0296, -0.3329, 0.0308, 0.1246}
4-IV	{0.0879, 0.0658, 0.2116, 0.0794, 0.2394, 0.2292, -0.1328, -0.0882, -0.3153, -0.3057, 0.0691, 0.2035}
0,1,2-V	{0.1557, 0.0533, 0.1783, 0.0599, 0.1853, 0.2543, -0.1502, -0.1091, -0.0309, -0.3185, 0.0493, 0.2168}
3-V	{0.1224, 0.0685, 0.2324, 0.0879, 0.1779, 0.2662,-0.1128, -0.0836, -0.0372, -0.2936, 0.0454, 0.2339}
4-V	{0.1354, 0.0680, 0.2030, 0.0778, 0.1419, 0.2866, -0.0985, -0.0841, -0.0254, -0.3873, 0.0615, 0.1711}

occurs only close to the trailing edge: the pressure gradient is not really steep, which means that a shock wave does not appear (see Figure 16(c)). These modifications are responsible for the reduction in inviscid drag coefficient of 2 counts, reported in Table 8. Moreover, the profile drag is lowered by reducing the wetted

American Institute of Aeronautics and Astronautics

Table 8. **Summary of the aerodynamic coefficients based on the same reference area. Drag coefficients are expressed in counts and C_{D0} includes also fins, pylons and nacelles**

Config.	C_m Constr.	α (°)	$C_L(\sim)$	$C_D(\sim)$	$C_{D0}(\sim)$	$C_{D_{inv}}(\sim)$	$M_{max}(\sim)$	$C_m(\sim)$	$C_L/C_D(\sim)$
0	-	1.4	0.26	131	60.3	70.7	1.47	-0.053	20.0
1	-	2.4	0.26	115	58.4	56.6	1.41	-0.024	22.8
2	$C_m > -0.015$	2.7	0.26	113	57.5	55.5	1.32	-0.014	23.3
3	$C_m > -0.010$	2.8	0.26	112	57.4	54.6	1.25	-0.009	23.5
4	$C_m > -0.015$	2.8	0.26	111	57.2	53.8	1.25	-0.014	23.7

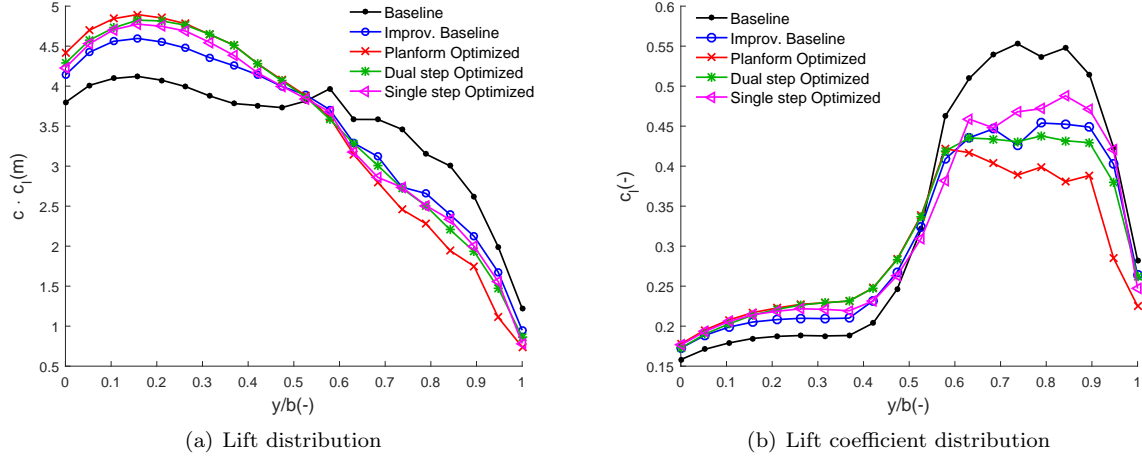(a) Lift distribution

(b) Lift coefficient distribution

Figure 15. **Spanwise distribution of lift and lift coefficient for five Flying V configurations.**

area (the wing area is 1.5% lower) and increasing the sweep angle. All the constraints are satisfied.

2. SU2 Euler Airfoil Optimization: from Config. 2 to Config. 3

The planform-optimized configuration is the starting point for the SU2 Euler airfoil optimization, as shown in Figure 3, in which the design variables are the 24 CST coefficients and 2 twist angles of profiles IV and V and the 9 rear airfoil parameters of sections I, II and III (Table 5). The design space is limited by the constraints reported in Table 3. In particular, the thickness to chord ratio of profiles IV and V (Figure 6) must be higher than 8.5% to avoid a really thin outer wing, which may involve a relevant weight penalty. This analysis is computationally more costly due to a larger amount of variables involved (35 compared to 10). The total time is 133.22 hours.

In Figure 15(a) the load distribution of the dual-step optimized Flying V (Config. 3, green line) is shown. The spanwise load is similar to the one of the planform-optimized configuration (Config. 2, red line). However, the local lift coefficient of the outboard wing is slightly higher and the load is reduced inboard (Figure 15(b)). The aerodynamic efficiency of the outboard wing is greatly improved by the airfoil optimization: the local drag coefficient decreases, as shown in Figure 17. It is noticeable that the green and red lines start diverging at $y/b = 0.6$, where section IV is positioned. In particular, the outboard portion of the wing is unconstrained and free to vary, whereas the inboard part is driven by the cabin parameters. The thickness to chord ratio of profiles IV and V is 8.6% and 9.5% respectively, hence the thickness constraint is respected.

In Figure 18, six different spanwise sections of the dual-step optimized Flying V (Config. 3, dotted lines) are compared to the planform-optimized ones (Config. 2, solid lines), together with the pressure coefficient distributions. The root airfoil, shown in Figure 18(a), is slightly modified and the trailing edge pressure recovery is smoother and less steep. The sections of Figure 18(b) and Figure 18(c) (in which the rear part of the airfoil only is allowed to change, see Section B) do not undergo meaningful modifications. In the outer-
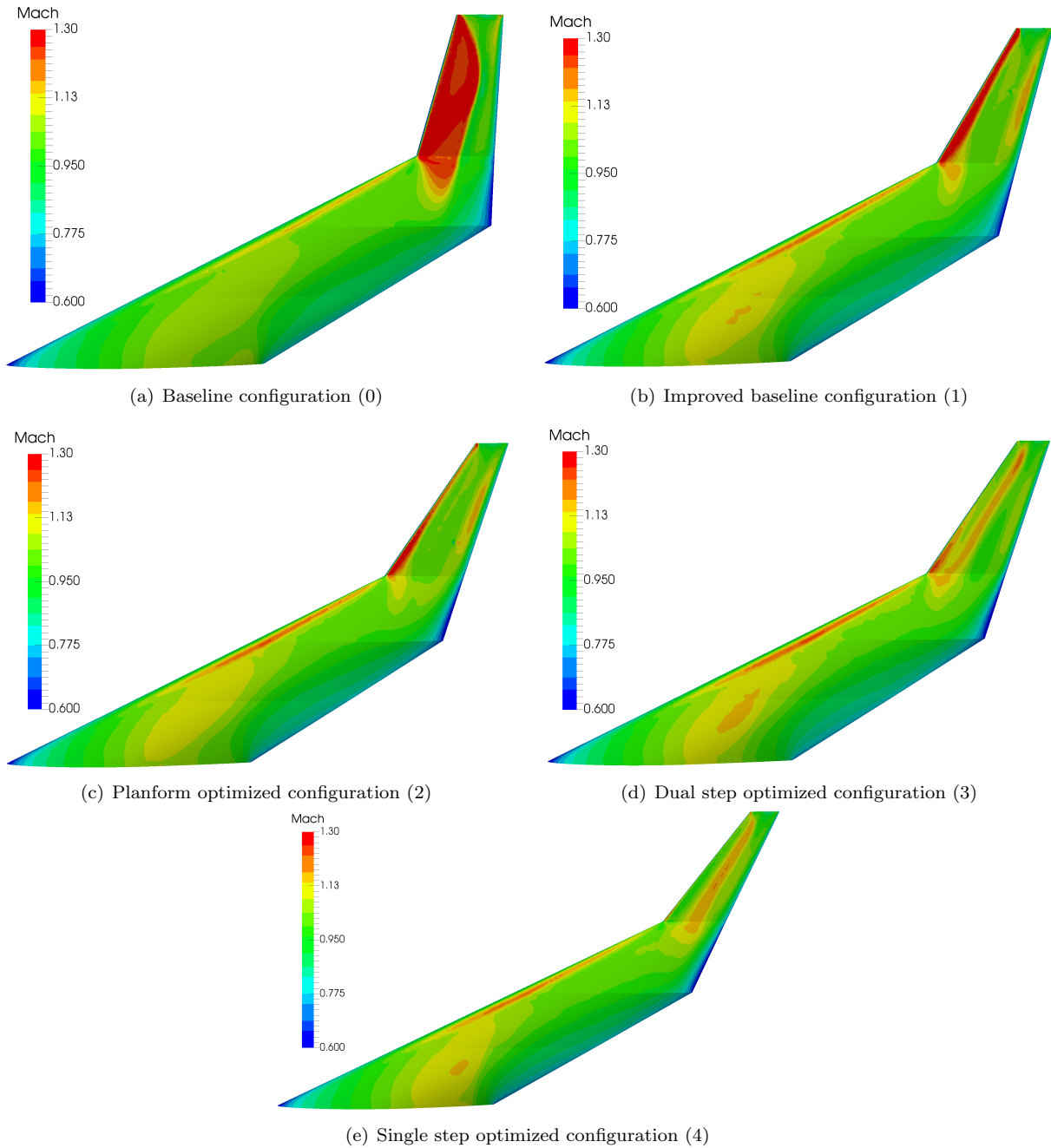
American Institute of Aeronautics and Astronautics

(a) Baseline configuration (0)

(b) Improved baseline configuration (1)

(c) Planform optimized configuration (2)

(d) Dual step optimized configuration (3)

(e) Single step optimized configuration (4)

Figure 16. Mach contours of the 5 configurations

wing airfoils, shown in Figures 18(d) to 18(f), three beneficial changes can be noticed. The leading-edge radius is smaller, which entails lower supervelocities and reduced maximum Mach over the surface (from 1.32 to 1.25, see Table 6). The rear airfoil curvature is reduced, hence the adverse pressure gradient is less steep. Furthermore, front loading is created and rear loading is slightly reduced. This helps reducing the pitch down moment. These modifications justify the higher aerodynamic efficiency of the outboard wing. This is appreciable in the Mach contours of Figure 16(d), where the supersonic flow area decreases considerably. This Flying V configuration results in a higher lift to drag ratio (23.5), obtained by saving 1 drag count. The total computational time of the dual step optimization (planform + airfoil) is 167 hours.
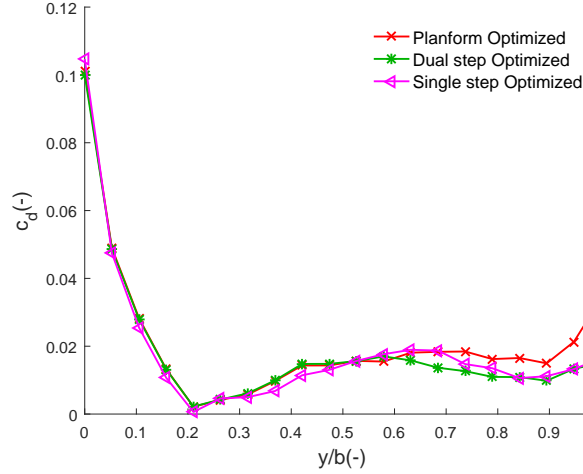
American Institute of Aeronautics and Astronautics

Figure 17. Local inviscid drag coefficient distribution: comparison between airfoils-optimized configuration and planform-optimized one

D. SU2 Single-Step Optimization: from Config. 1 to Config. 4

As shown in Figure 3, also a single-step SU2 optimization is applied to the improved-baseline configuration (Config. 1). The variables and inequality constraints are reported in Table 5. The total computational time is 125 hours, slightly lower than the airfoil optimization time, mentioned in Section 2: in particular, the nine rear-airfoil parameters ($\bar{y}_{\mathrm{rear}}$) are not involved in this analysis in order to reduce the computational effort.

The lift distribution of the single-step optimized configuration (Config.4, magenta line in Figure 15(a)) is in agreement with the dual-step optimized configuration (Config. 3, green line). On the other hand, the outboard wing of this configuration is more slender than the dual-step optimized one, as can be seen in Figure 16(e), which entails a higher outboard lift coefficient (Figure 15(b)). The wing area resulting from the single-step optimization is similar to the planform-optimized Configuration (about 883 m², Table 6). The sweep angles are slightly higher and the nose-down washout is still present. The pressure-coefficient distributions of the single-step-optimized configuration are compared to the dual-step optimized configurations in Figure 19. Again, front loading is introduced and the trailing-edge pressure recovery is less steep. Profile V (Figure 6) of the two configurations is really similar, as reported in Table 7 and displayed in Figure 19(d). The local inviscid drag coefficient is shown in Figure 17 (based on the same reference area): it features a trend similar to the dual-step optimized Flying V, it is slightly lower from $y/b = 0.3$ to $y/b = 0.55$ and higher between $y/b = 0.55$ to $y/b = 0.85$. The maximum Mach number over the wing is 1.25 (Table 8), which represents a remarkable achievement. The total drag coefficient is further reduced by 1 count (Table 8), while all constraints are satisfied. In particular, the thickness-to-chord ratio of profiles IV and V is 9.5% and 9.2% respectively favoring the single-step design over the dual-step design from a structural point of view. In a nutshell, the single step optimization provides better results at a lower computational cost if compared to the dual-step procedure.

E. Fin Sizing Results

The fin sizing procedure, described in Section A, is subsequently applied to the single step optimized configuration. The variables, bounds and optimum values are reported in Table 9.The optimization constraints are represented by the three driving requirements outlined in Table 1. In order to check the directional static stability requirement, the tail-off directional stability derivative at the most aft center of gravity location (obtained with a 2.5% static margin) is computed by SU2 and it is equal to -0.0187 1/rad. This means that the Flying V is directionally unstable without a vertical surface behind the center of gravity. The thick inboard wing, which is ahead of the center of gravity, has a destabilizing effect. The other two constraints are related to the required rudder deflection at two critical conditions: OEI condition at take-off and maximum crosswind at landing conditions.

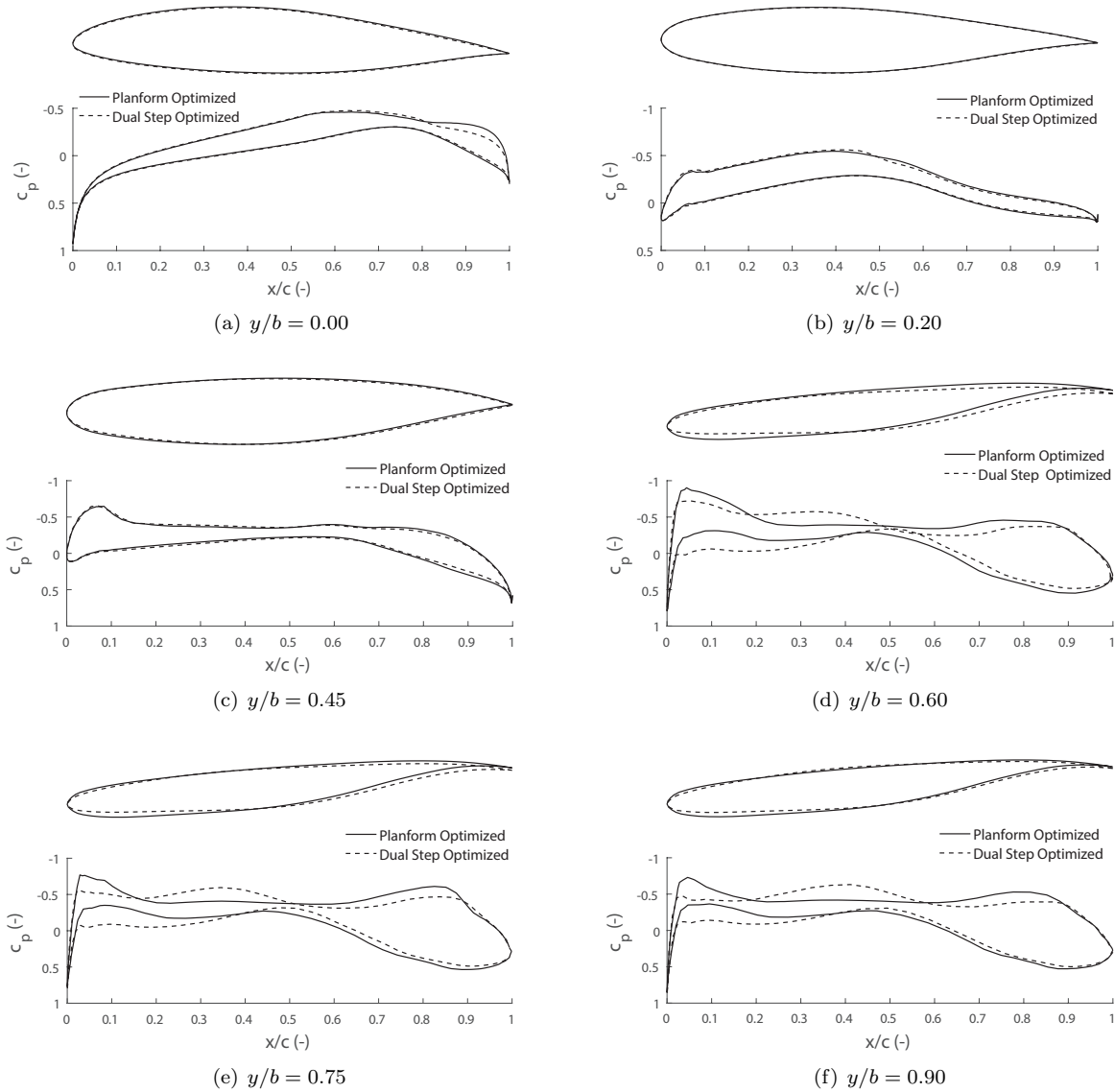The fin resulting from the design procedure has a surface area of 13 m²: considering that two twin fins

American Institute of Aeronautics and Astronautics

Figure 18. SU2 Euler airfoil optimization: comparison of pressure coefficient distributions at different spanwise locations (M = 0.85, C_L=0.26)

Table 9. Fin design variables, bounds and optimum values.

Variable	Initial value	Bounds	Optimum value
Λ_{fin} (deg)	30	$20 < \Lambda < 50$	36
A_{fin} ($\sim$)	2.0	$1.0 < A < 3.0$	2.3
λ_{fin} ($\sim$)	0.60	$0.45 < \lambda < 0.70$	0.45

are used, the total area is 26 m². With the engines line of thrust located at $y/b = 0.1$, the OEI condition is not the most critical condition, whereas the directional stability target is the most demanding. The optimum design variables are reported in Table 9: the taper ratio is on the lower bound where the area is minimum, the aspect ratio is 2.3 in order to guarantee the required lift slope and the sweep angle is slightly higher than the initial value to ensure a longer arm. Since the design is purely aerodynamic, the impact of the taper ratio on the structure is not taken into account, hence a multidisciplinary analysis will be needed. A sweep angle of 36° is also beneficial to handle maximum sideslip angles: the value is within the range proposed by
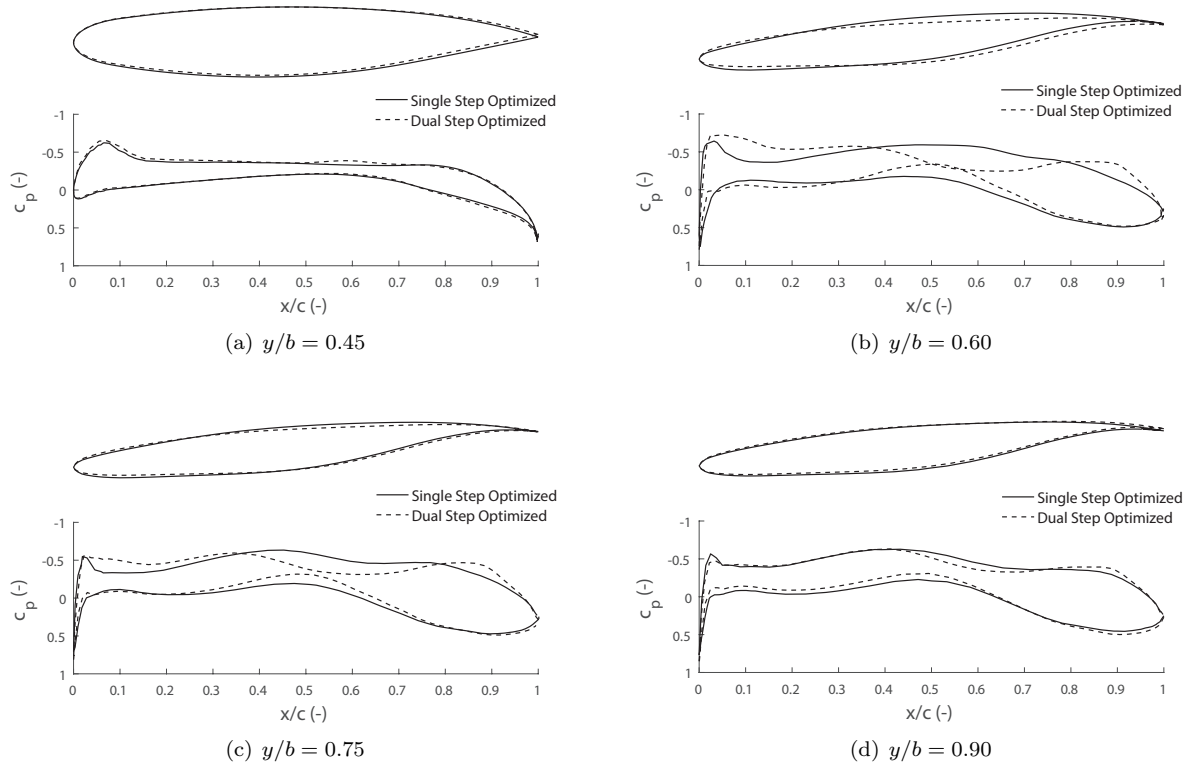
American Institute of Aeronautics and Astronautics

(a) $y/b = 0.45$

(b) $y/b = 0.60$

(c) $y/b = 0.75$

(d) $y/b = 0.90$

Figure 19. SU2 Euler single step optimization: comparison of pressure coefficient distributions at 4 spanwise locations (M = 0.85, C_L=0.26)

Obert[25] for jet transport aircraft.

The required fins area is about 50% higher than the one predicted by Benad,[20] equal to 16 m², based on a dynamic stability study, in which the derivatives are computed by a vortex-lattice method. If the static stability constraint is relaxed (neutral stability required), the OEI condition becomes the most critical, therefore the surface area is slightly reduced to 24 m². If the neutral stability constraint is the only one active, the total area required is 20 m²: in this case the rudder deflection required in OEI condition is 28°, higher than the maximum allowed. The fin of Table 9 is used to analyse the full Flying V. Being the tail-off stability derivative approximately the same for the different configurations, the area (hence the profile drag) of the fins of the different configurations is within a 5% difference. Therefore, their n prole drag is within the same deviation.

F. Results Summary

In this section, the overall results of the resulting full Flying V configurations (with fins) are discussed. The drag polar is displayed in Figure 20(a). Since the goal of the analysis is to evaluate the aerodynamic cruise performances, only conditions relatively close to the design point are shown. The drag coefficient at the cruise point is reduced by the multi-fidelity design space exploration by 16 counts and then 4 additional drag counts are saved with the optimization procedures. It is also important to note that the distance between the curves increases at high lift coefficients: it means that the baseline configuration deteriorates more rapidly. This is even more appreciable in Figure 20(b), where the maximum lift-to-drag ratio is plotted versus the lift coefficient: it can be obtained when the Flying V is trimmed without any elevon deflection. In particular, the maximum lift-to-drag ratio of the optimized configurations is almost flat above the design lift coefficient, whereas it decreases in case of the configurations 1 and 2 (defined in Figure 3). As expected, the Flying V is aerodynamically more efficient at higher lift coefficients, i.e. at higher altitudes and at the same Mach number. For instance, even though the Flying V is optimized at the lift coefficient of 0.26, the highest lift-to-drag ratio of the dual-step optimized Flying V is attained at a lift coefficient that is 10% higher than the design lift coefficient, at an altitude of 13,600 m.
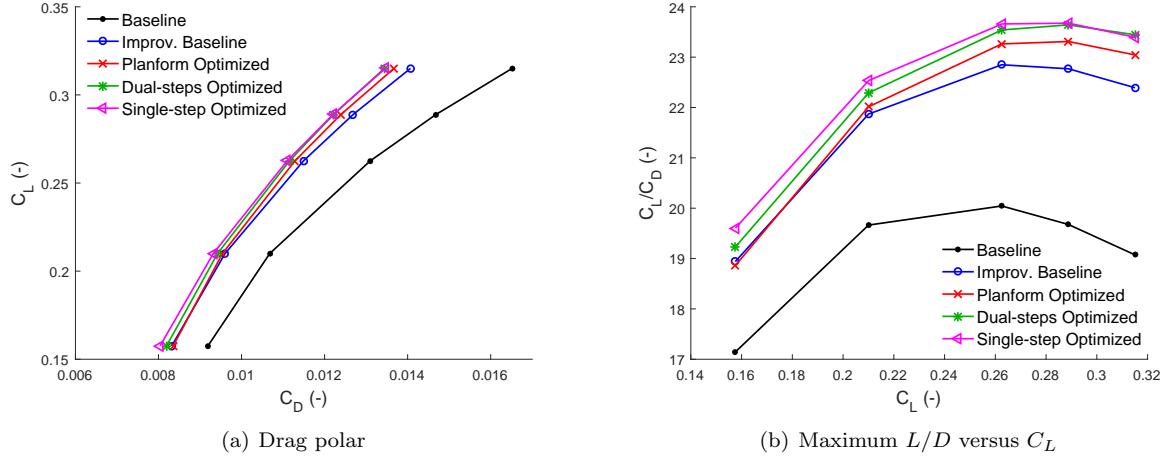
American Institute of Aeronautics and Astronautics

(a) Drag polar

(b) Maximum L/D versus C_L

Figure 20. Aerodynamic properties of five Flying V designs

However, the selection of the cruise altitude involves various disciplines and transport airplanes usually end up flying lower due to some important reasons. First of all, the engine available thrust decreases at higher altitudes. In addition, the pressure difference between inside and outside the pressurised cabin hull is bigger. This usually requires a more resistant structure: perhaps, at this altitude the difference might be negligible. Finally, the aircraft is subjected to a buffet limit, that can be approached at relatively high Mach numbers and lift coefficients. Therefore, flying at higher lift coefficients decreases the buffet margin. In particular, the maximum local Mach over the wing goes up to 1.3, which is above the limit of 1.25 imposed by design guidelines.

G.   Results Comparison with NASA CRM

The NASA Common Research Model (CRM) is taken as a representative, modern tube-and-wing aircraft with known aerodynamic properties. The same aerodynamic analysis method as applied to the Flying V aircraft is also applied to the NASA CRM to estimate its lift-to-drag ratio. The geometry of the NASA CRM used in the simulation features the wing, fuselage, horizontal tail plane and wing-body fairing. Hence, engine nacelles, pylons and vertical tail are not included in the SU2 simulations. The same holds for the Flying V model. They are analyzed by the viscous module only. Moreover, in order to make a fair comparison, the following expedients are adopted. The same nacelle and pylon profile drag is assumed and the vertical tail is included (the geometry is extracted from the CAD created by ONERA[3]). Moreover, the same flight conditions, i.e. Mach number, air temperature and pressure are considered. Finally, a similar grid refinement is adopted as used on the Flying V aircraft.

The results are reported in Table 10. The profile drag of the NASA CRM computed by the viscous module is equal to 140 drag counts: this corresponds to a parasite drag area of 5.4 m^2, 6% higher than the parasite drag area of the Flying V (5.1 m^2). This difference is the result of the larger wetted area of the NASA CRM. The inviscid drag computed by SU2 is 124 counts. Therefore, the lift-to-drag ratio of the Flying V (23.7) is 25% higher than the L/D of the NASA CRM (18.9).

Table 10. Comparison of aerodynamic properties between Flying V and NASA CRM.

	$C_L(\sim)$	C_D (cts)	C_{D0} (cts)	$C_{D0}S_{\text{ref}}(\text{m}^2)$	$C_{D_{\text{inv}}}$ (cts)	$C_L/C_D(\sim)$
Flying V (config. 4)	0.26	111	57	5.1	54	23.7
NASA CRM	0.5	264	140	5.4	124	18.9

---

[c]NASA   Common   Research   Model.   Retrieved   on   September   20th,   2016   from https://commonresearchmodel.larc.nasa.gov/geometry/vertical-tail-geometry/

American Institute of Aeronautics and Astronautics

V. Conclusions and Recommendations

The goal of the present paper is to present an optimized aerodynamic design of a Flying V aircraft, and compare its aerodynamic properties in clean configuration to a modern tube-and-wing aircraft. The maximum obtained lift-to-drag ratio of the optimized Flying V configuration in this study is 23.7 at the cruise altitude and Mach number. This is close to the estimation of 25, which was assumed in the conceptual design phase. In addition, a plateau in aerodynamic efficiency is shown around the design lift coefficient allowing small deviations in wing loading without a change in aerodynamic efficiency. The Flying V aircraft is also compared to the NASA Common Research Model by using the aerodynamic analysis method. The maximum lift-to-drag ratio of this benchmark configuration is 18.9 resulting in a 25% higher aerodynamic efficiency for the Flying V aircraft than the NASA Common Research Model.

While this study has successfully shown a relatively high aerodynamic efficiency of the Flying V aircraft, additional research is required to investigate other aspects concerning the overall design of the Flying V including its maximum lift coefficient, the effect of the twin fins on the aerodynamic efficiency, and its weight distribution. These aspects are currently being evaluated by the authors.

Acknowledgments

References

[1] Martinez-Val, R., Perez, E., Puertas, J., and Roa, J., "Optimization of planform and cruise conditions of a transport flying wing," in "Proceedings of the Institution of Mechanical Engineers, Part G: Journal of Aerospace Engineering," Vol. 224, 2010, pp. 1243–1251.

[2] Torenbeek, E., "Blended Wing Body and All-Wing Airliners," in "European Workshop on Aircraft Design Education (EWADE)," Samara, 2007.

[3] Martiénez-Val, R., Pérez, E., Alfaro, P., and Pérez, J., "Conceptual design of a medium size flying wing," in "Proceedings of the Institution of Mechanical Engineers, Part G: Journal of Aerospace Engineering," Vol. 221, 2007, pp. 57–66.

[4] Bolsunovsky, A. L., Buzoverya, N. P., Gurevich, B. I., Denisov, V. E., Dunaevsky, A. I., Shkadov, L. M., Sonin, O. V., Udzhuhu, A. J., and Zhurihin, J. P., "Flying wing - Problems and decisions," *Aircraft Design*, Vol. 4, No. 4, 2001, pp. 193–219.

[5] Martinez-Val, R., Palacin, J. F., and Perez, E., "The evolution of jet airliners explained through the range equation," in "Proceedings of the Institution of Mechanical Engineers, Part G: Journal of Aerospace Engineering," Vol. 222, 2008, pp. 915–919.

[6] Wood, R. M. and Bauer, S. X. S., "Flying Wings/ Flying Fuselages," in "39th AIAA Aerospace Sciences Meeting & Exhibit," Reno, January, 2001.

[7] Martinez-Val, R., "Flying Wings. A New Paradigm for Civil Aviation?" *Acta Polytechnica*, Vol. 47, No. 1.

[8] Denisov, V., Shkadov, L., and Chernyshev, S., "The Flying Wing Concept - chances and risks," in "AIAA International Air and Space Symposium and Exposition: The Next 100 Years," Dayton, July, 2003, pp. 1–11.

[9] Mialon, B., Fol, T., and Bonnaud, C., "Aerodynamic optimization of subsonic flying wing configurations," in "20th AIAA Applied Aerodynamics Conference," St. Louis, June, 2002, pp. 1–7.

[10] Saeed, T. I. and Graham, W. R., "Design Study for a Laminar-Flying-Wing Aircraft," *Journal of Aircraft*, Vol. 52, No. 5, 2015, pp. 1373–1385.

[11] Zhang, M., Rizzi, A., Meng, P., Nangia, R., Amiree, R., and Amoignon, O., "Aerodynamic Design Considerations and Shape Optimization of Flying Wings in Transonic Flight," in "12th AIAA Aviation Technology, Integration, and Operations (ATIO) Conference and 14th AIAA / ISSM," Indianapolis, September, 2012, pp. 1–17.

[12] Mader, C. A., "Stability-Constrained Aerodynamic Shape Optimization of Flying Wings," *Journal of Aircraft*, Vol. 50, No. 5.

[13] Liebeck, R. H., "Design of the Blended Wing Body Subsonic Transport," *Journal of Aircraft*, Vol. 41, No. 1, 2004, pp. 10–25.

[14] Roman, D., Gilmore, R., and Wakayama, S., "Aerodynamics of high-subsonic blended-wing-body configurations," in "41st Aerospace Sciences Meeting and Exhibit," Reno, January, 2003, pp. 1–9.

[15] Qin, N., Vavalle, A., Le Moigne, A., Laban, M., Hackett, K., and Weinerfelt, P., "Aerodynamic considerations of blended wing body aircraft," *Progress in Aerospace Sciences*, Vol. 40, No. 6, 2004, pp. 321–343.

[16] Qin, N., Vavalle, A., Le Moigne, A., Laban, M., Hackett, K., and Weinerfelt, P., "Aerodynamic Studies for Blended Wing Body Aircraft," in "9th AIAA/ISSMO Symposium on Multidisciplinary Analysis and Optimization," Atlanta, September, 2002, pp. 1–11.

[17] Pambagjo, T., Nakahashi, K., Obayashi, S., and Matsushima, K., "Aerodynamic design of a medium size blended-wing-body airplane," in "39th Aerospace Sciences Meeting and Exhibit," Tohoku, January, 2001.

[18] Reist, T. A. and Zingg, D. W., "Aerodynamic Design of Blended Wing-Body and Lifting-Fuselage Aircraft," in "34th AIAA Applied Aerodynamics Conference," Washington, D.C., 2016.

[19]Li, P., Zhang, B., Chen, Y., Yuan, C., and Lin, Y., "Aerodynamic design methodology for blended wing body transport," *Chinese Journal of Aeronautics*, Vol. 25, No. 4, 2012, pp. 508–516.

[20]Benad, J., "Design of a commercial aircraft for high-subsonic speed as a flying wing configuration," Tech. rep., Airbus, Berlin, 2015.

[21]Benad, J., "The Flying V: An entirely new aircraft configuration," , 2015.

[22]Torenbeek, E., *Synthesis of Subsonic Airplane Design*, Delft University Press, 1976.

[23]Vassberg, J. C., DeHaan, M. A., Rivers, S. M., and Wahls, R. A., "Development of a Common Research Model for Applied CFD Validation Studies," in "26th AIAA Applied Aerodynamics Conference," Honolulu, August, 2008.

[24]Storn, R. and Price, K., "Differential Evolution: A Simple and Efficient Heuristic for Global Optimization over Continuous Spaces," *Journal of Global Optimization*, Vol. 11, 1997, pp. 341–359.

[25]Obert, E., *Aerodynamic design of transport aircraft*, IOS Press BV, 2009.

[26]Sadraey, M. H., *Aircraft design: A systems engineering approach*, John Wiley \& Sons, 2012.

[27]Vos, R., Geuskens, F. J. J. M. M., and Hoogreef, M. F. M., "A New Structural Design Concept for Blended Wing Body Cabins," in "53rd AIAA/ASME/ASCE/AHS/ASC Structures, Structural Dynamics and Materials Conference," Honolulu, April, 2012.

[28]Selvan, K. M., "On the effect of Shape Parameterization on Aerofoil Shape Optimization," *IJRET: International Journal of Research in Engineering and Technology*.

[29]Palacios, F., Colonno, M. R., Aranake, A. C., Campos, A., Copeland, S. R., Economon, T. D., Lonkar, A. K., Lukaczyk, T. W., Taylor, T. W. R., and Alonso, J. J., "Stanford University Unstructured (SU 2): An open-source integrated computational environment for multi-physics simulation and design ." in "51st AIAA Aerospace Sciences Meeting including the New Horizons Forum and Aerospace Exposition," Grapevine, January, 2013.

[30]Gur, O., Mason, W. H., and Schetz, J. A., "Full Configuration Drag Estimation," in "27th AIAA Applied Aerodynamics Conference," San Antonio, June, 2009.

[31]Raymer, D. P., *Aircraft Design: A Conceptual Approach*, American Institute of Aeronautics and Astronautics, 2004.

[32]Chan, W. M., Gomez, R. J., Rogers, S. E., and Buning, P. G., "Best practices in overset grid generation," in "32nd AIAA Fluid Dynamics Conference," St. Louis, 2002.

[33]Roskam, J., *Airplane Design: Preliminary Sizing of Airplanes*, DARcorporation, 1985.

[34]Woodard, P. R., Batina, J. T., and Yang, H. T. Y., "Quality assessment of two and three-dimensional unstructured meshes and validation of an upwind Euler flow solver," *NASA Technical Memorandum 104215*.

[35]Schmitt, V. and Charpin, F., ""Pressure Distributions on the ONERA-M6-Wing at Transonic Mach Numbers," Experimental Data Base for Computer Program Assessment," Tech. rep., Fluid Dynamics Panel Working Group 04, AGARD AR 138, 1979.

[36]Durrani, N. and Qin, N., "Comparison of RANS, DES and DDES results for ONERA M-6 Wing at transonic flow speed using an in-house parallel code," in "49th AIAA Aerospace Sciences Meeting," Orlando, January, 2011.

[37]Ueno, M., Yamamoto, K., Tanaka, K., Murayama, M., and Tognaccini, R., "Far-Field Drag Analysis of NASA Common Research Model Simulations by JAXA," in "AIAA Computational Fluid Dynamics Conference," Honolulu, June, 2011, pp. 1–14.

[38]Whitcomb, R. T., "Review of NASA supercritical airfoils," in "9th International Council of the Aeronautical Sciences Congress," Haifa, 1974.

[39]Vos, R. and Farokhi, S., *Introduction to Transonic Aerodynamics*, Springer, 2015.